J. Fluid Mech. (1999), *vol.* 381, *pp.* 239–269. Printed in the United Kingdom

Evolution of isolated vortices in a rotating fluid of finite depth

By P. ORLANDI[1] AND G. F. CARNEVALE[2]

[1]Università di Roma 'La Sapienza' Dipartimento di Meccanica e Aeronautica, via Eudossiana n^o 18 00184 Roma Italy
[2]Scripps Institution of Oceanography University of California, San Diego, La Jolla, CA 92093, USA

(Received 24 December 1997 and in revised form 21 September 1998)

Laboratory experiments have shown that monopolar isolated vortices in a rotating flow undergo instabilities that result in the formation of multipolar vortex states such as dipoles and tripoles. In some cases the instability is entirely two-dimensional, with the vortices taking the form of vortex columns aligned along the direction of the ambient rotation at all times. In other cases, the vortex first passes through a highly turbulent three-dimensional state before eventually reorganizing into vortex columns. Through a series of three-dimensional numerical simulations, the roles that centrifugal instability, barotropic instability, and the bottom Ekman boundary layer play in these instabilities are investigated. Evidence is presented that the centrifugal instability can trigger the barotropic instabilities by the enhancement of vorticity gradients. It is shown that the bottom Ekman layer is not essential to these instabilities but can strongly modify their evolution.

1. Introduction

Laboratory experiments on the evolution of isolated vortices in rotating flow have provided many interesting examples of instabilities which lead to the formation of stable multipolar vortices. The transformations of axially symmetric vortices into tripoles and dipole pairs are impressive examples of this process (cf. Kloosterziel & van Heijst 1991; van Heijst, Kloosterziel & Williams 1991). A complete theoretical understanding of this phenomenon would require a fully three-dimensional instability theory, but this is not at present available. However, much insight can be obtained by considering the combined effect of barotropic (i.e. two-dimensional) instability and centrifugal instability, which involves three-dimensional overturning of the fluid.

An important effect of rotation is that it tends to suppress variation of the flow in the direction along the axis of rotation. In rotating tank experiments, this 'two-dimensionalization' tends to make the vortices evolve toward columnar structures aligned along the direction of the tank's rotation axis. If a flow is completely two-dimensional, then except for the direction of rotation, there can be no difference between the evolution of cyclones and anticyclones, because in the equations of two-dimensional advection there are no terms that can break this symmetry. The effect of two-dimensionalization by rotation is commonly associated with the Taylor–Proudman theorem. This theorem states that the variation along the direction of the axis of rotation will vanish to the extent that, in the rotating reference frame, the flow is stationary and nonlinear inertial effects can be neglected. In Carnevale *et al.* (1997*a*)

we investigated how the columnar state is achieved from initially three-dimensional vortices. This also involved studying the stability of nearly columnar vortices, and for that we took vorticity profiles that were single signed and monotonically decreasing as a function of the distance from the axis of the vortex. This monotonic type of profile was chosen so as to avoid barotropic instabilities because we wanted to focus on the three-dimensional centrifugal instability and two-dimensional stability theory showed us that such flows are barotropically stable. The linear stability of such vortices is given by the Rayleigh inflection point theorem (cf. Drazin & Reid 1981), and this is strengthened by nonlinear stability theorems of the Arnol'd type (cf. Dritschel 1988; Carnevale & Shepherd 1990). However, isolated vortices cannot have such a monotonic vorticity profile, and hence are subject to two-dimensional or barotropic instabilities as well as the three-dimensional centrifugal instability. It is to this problem of the combined effect of barotropic and centrifugal instability that we now turn.

By an isolated vortex, we mean a vortex for which the velocity field falls off faster than $1/r$ where r is the distance from the axis of the vortex. For a columnar vortex this would mean that the circulation in any horizontal plane must vanish. Note that we will refer to the direction aligned along the ambient rotation axis as 'vertical'. An idealization of the vortices created in the laboratory experiments is a vortex that is axially symmetric with no variation in the vertical, with a core of one sign of vorticity surrounded by an annulus of oppositely signed vorticity such that the integral of the vorticity in all horizontal planes vanishes. The behaviour of this kind of vortex is very different from that of the vortex with a single sign of vorticity. The latter vortices do not undergo the barotropic type of instability that produces the multipolar end states (cf. Kloosterziel & van Heijst 1991; Carnevale *et al.* 1997*a*). For the isolated vortex the Rayleigh inflection point criterion is satisfied, and so a two-dimensional (i.e. barotropic) instability is possible. Depending on the exact distribution of vorticity, the isolated vortex will be unstable to normal modes of angular dependence proportional to $\cos(n\theta)$ where θ is the azimuthal angle in a cylindrical geometry and n is an integer. In numerical simulations the linear instabilities can be shown to lead to the formation of multipolar structures such as the tripole ($n = 3$), quadrapole ($n = 4$), pentapole ($n = 5$) etc. in which a core vortex of one sign of vorticity is surrounded by satellite vortices of the opposite sign (cf. Carnevale & Kloosterziel 1994; Morel & Carton 1994). Most of these structures are unstable and typically break up into dipoles and monopoles. A notable exception is the tripole which is very stable (Carton & Legras 1994) and is readily produced in rotating tank experiments (van Heijst & Kloosterziel 1989). The quadrupole is less robust, but appears stable in numerical simulations and has been created as a metastable state in rotating tank experiments (Kloosterziel & van Heijst 1991; Carnevale & Kloosterziel 1994). We will discuss these structures in more detail in later sections.

The laboratory set up used in Kloosterziel & van Heijst (1991, 1992) and van Heijst *et al.* (1991) consists of a rotating table on which is placed a cylindrical tank. Rotation combined with the bottom boundary and the free surface of the fluid tends to diminish motion in the vertical direction throughout the tank. Thus the rotation, if sufficiently strong, permits us to perform experiments which are essentially two-dimensional, that is with no variation in the vertical, and hence to study purely barotropic instabilities. The initial condition in these experiments was prepared by stirring in a hollow cylinder placed in the centre of the tank. By stirring in the direction of the rotation of the tank, or in the opposite direction, one can smoothly create a confined cyclone or anticyclone respectively. Once the motion in

the confining cylinder becomes fairly two-dimensional, the hollow cylinder is removed vertically, leaving behind an isolated vortex, whose subsequent evolution is observed. On removing the hollow inner cylinder, some three-dimensional motion is generated, which, when the vortex is centrifugally unstable, can become very vigorous. There is usually then a transitory turbulent period before the flow returns to a two-dimensional state.

One of the most intriguing facets of this research is the asymmetry between the cyclones and anticyclones. If the strength of the vortices is sufficiently weak, then, by the Taylor–Proudman theorem (cf. Pedlosky 1979), we can expect little difference between cyclones and anticyclones. However, for stronger amplitudes, their behaviours can be very different. In the laboratory experiments reported in the current literature, it was found that tripoles could easily be generated from cyclones, but not from anticyclones. The anticyclones instead would break into dipole pairs ('double-dipole instability'), sometimes after first forming intermediate tripolar or quadrupolar structures (cf. Kloosterziel & van Heijst 1991; van Heijst *et al.* 1991; Orlandi & van Heijst 1992; Carnevale & Kloosterziel 1994). In contrast, the double-dipole instability for a cyclone could be produced experimentally in only one very special case (van Heijst *et al.* 1991). For that case, the authors of the study concluded that the core cyclonic vortex was initially produced in such a way as to have a vorticity profile that was itself barotropically unstable.

Previous investigations have led to two important hypotheses that may help explain the asymmetry in behaviour between the cyclones and anticyclones. It was obvious in the experiments that when the anticyclones were released, they underwent centrifugal instability (cf. Kloosterziel & van Heijst 1991), and it was only after a period of decay of the resulting three-dimensional turbulence that two-dimensional columnar structures re-emerged. The cyclones, on the other hand, suffered only a small amount of three-dimensional disturbance by the removal of the confining cylinder, and remained predominantly two-dimensional at all times. Kloosterziel & van Heijst (1991) suggested that the centrifugal instability might in some way prevent the flow from achieving the right conditions for tripole formation and that the lack of the centrifugal instability in the cyclonic case somehow precludes the double-dipole instability (in all cases in which the core cyclonic vortex itself is not barotropically unstable). Alternatively, Kloosterziel & van Heijst (1991) suggested that within the confining cylinder, the action of a bottom Ekman layer generates vorticity in such a way as to favour the double-dipole instability for the anticyclone and the tripole instability for the cyclone. This seemed plausible because the strength of Ekman layer pumping is not simply proportional to the amplitude of the vorticity, but depends on it in a nonlinear way (Wedemeyer 1964), which means that Ekman pumping can change the profile of the vorticity. In an attempt to determine the importance of the Ekman layer effect in their experiments, Kloosterziel & van Heijst (1992) performed a series of experiments in which the effects of the bottom boundary layer were minimized by introducing a thin layer of fluid denser than the main layer at the bottom of the tank. In this case it seems the cyclones were stable, leading to the speculation that the instability of the cyclones relied on the Ekman effect, although effects of the deformation of the surface between the two layers clouds the interpretation of the result.

Our main goal here is to investigate these and subsidiary hypotheses about the effects of the centrifugal instability and the Ekman layer to determine their validity in explaining the behaviour of vortices in a rotating environment. Our investigation primarily involves a series of three-dimensional numerical experiments on flows with

differing boundary conditions, with which we can explore these phenomena more carefully than was possible in the laboratory experiments described above. In the laboratory experiments, with the stirring method discussed above, it was difficult to know the initial strength and vorticity profile of the vortices relative to the background (i.e. the initial Rossby number). In some cases, the strength and even the horizontal velocity field was measured and reported, but, especially in the centrifugally unstable anticyclone cases, this information is usually lacking. In contrast, in the numerical simulations, we have control over the initial conditions and have been able to examine a number of cases spanning a large range of Rossby numbers. One of the more difficult fields to measure in the laboratory is the vorticity field of the flow. Estimates of the vertical vorticity at the surface of the flow have been made in some cases from measurements of the velocities of particles dispersed on the surface, but these estimates seem very inaccurate. Also there are no measurements of the horizontal components of vorticity, which are essential to understanding the effects of centrifugal instability, anywhere in the flow. The original purpose of the laboratory experiments was the examination of the two-dimensional dynamics of vortices. Thus there was no-visualization and very little other information on the three-dimensional structure of the vortices. One great advantage of the numerical simulations is the ability to examine all components of the vorticity field at all times during the evolution.

Further, in the numerical simulations we can change the bottom boundary condition so as to include or exclude the effects of the Ekman layer. Thus we have performed simulations with periodic and slip boundary conditions which exclude the Ekman layer to test hypotheses about its importance in the experiments without introducing the complications of a bottom layer of different density as in the laboratory. For the simulations with a no-slip bottom boundary condition, we introduced a variable mesh so that we could resolve the Ekman layer well. It was important to examine the Ekman effect for a wide range of Rossby numbers, because there was ambiguity about the initial Rossby numbers in many of the laboratory experiments and because only at very low Rossby number is there a good theoretical understanding of the structure of the Ekman layer, while many of the experiments have been performed with high Rossby numbers where we have no guiding theory.

In the next section, we will discuss some fundamental considerations concerning pure barotropic and pure centrifugal instability that will be important in interpreting the results for the laboratory experiments and numerical simulations. Then in §3, we will consider various aspects of the numerical simulations without Ekman-layer effects. In §4, we will show the results of three-dimensional flow simulations that resolve the Ekman layer.

2. Fundamental aspects of the barotropic and centrifugal instabilities

Barotropic instability of isolated vortices has been the subject of a number of studies. A useful model for the vorticity of a vortex of limited horizontal extent that has been used in several studies (cf. Carton, Flierl & Polvani 1989; Orlandi & van Heijst 1992; Carnevale & Kloosterziel 1994) is given by

$$\omega_z = \omega_0(1 - \tfrac{1}{2}\alpha\rho^\alpha)\mathrm{e}^{-\rho^\alpha}, \tag{2.1}$$

where ω_z is the vorticity relative to the background ambient rotation, and ω_0 is the amplitude of the vortex at $r = 0$. Also $\rho = r/(\sqrt{2}\sigma)$ with σ defining a horizontal length scale of the vortex. Throughout the paper, we will use a cylindrical coordinate system with independent spatial variables denoted by r, θ and z, with the background

rotation vector $\boldsymbol{\Omega} = \Omega\hat{\boldsymbol{z}}$ aligned either parallel or antiparallel to the z-axis depending on the sign of Ω. The profile (2.1) is a convenient choice since, by adjusting the steepness exponent α, it can be easily fitted to a wide variety of vorticity profiles observed in nature and in the laboratory experiments. It is an isolated profile in the sense that the circulation or total vorticity integrated over the plane vanishes. This means that the associated velocity field will fall off more rapidly than $1/r$ in the far field. Specifically, for this profile we have

$$v_\theta = \tfrac{1}{2}\omega_0 r \mathrm{e}^{-\rho^\alpha}. \tag{2.2}$$

Note that the vorticity ω_z changes sign at the radius given by

$$r = r_\times = \sqrt{2}\sigma \left[\frac{2}{\alpha}\right]^{1/\alpha}. \tag{2.3}$$

Having introduced the basic profile (2.1), we can now define precisely the important non-dimensional numbers for our problem. We define the Reynolds number as

$$Re = \frac{\omega_0 \sigma^2}{\nu}, \tag{2.4}$$

where ν is the kinematic velocity. The rotation number is defined by

$$N = \frac{2\Omega}{\omega_0}. \tag{2.5}$$

We will take ω_0 to be positive always, and Ω to be a signed quantity so that $N > 0$ refers to a cyclone and $N < 0$ to an anticyclone. Here we are using rotation number N instead of the Rossby number $Ro = 1/|N|$ since this will simplify much of the discussion. In addition to these two non-dimensional numbers, we will have occasion to refer to two important time scales, the advective and the Ekman time scales. The advective time scale is given by

$$t_a = \frac{1}{\omega_0}, \tag{2.6}$$

and the Ekman time scale by

$$t_E = \frac{D}{(\nu\Omega)^{1/2}}, \tag{2.7}$$

where D is the depth of the fluid, that is the size of the computational domain in the vertical direction. The aspect ratio σ/D will be taken to be $1/\pi$ in all three-dimensional simulations presented below. The aspect ratios used in the laboratory experiments cited above vary from about 0.2 to 3, but it is beyond the scope of the present work to consider such a wide range of aspect ratios. Except where explicitly stated otherwise, numerical values of all physical quantities will be given with time scales in units of t_a and length scales in units of σ.

In figure 1, we show the results from a two-dimensional numerical linear stability analysis of the vorticity profile given in (2.1). The growth rates were computed by numerical simulation of the evolution of the vorticity field linearized about the profile given in equation (2.1). The instability was initiated by adding a small perturbation with azimuthal dependence given by $\cos(n\theta)$ with n a positive integer (for details see Carnevale & Kloosterziel 1994). The graph shows that for small values of α the profile is linearly stable. For α greater than about 1.85 the profile is unstable to mode $n = 2$ perturbations. For successively higher values of α, higher-order modes are unstable. In other words, the 'steeper' the profile, the larger the number of modes that can grow.

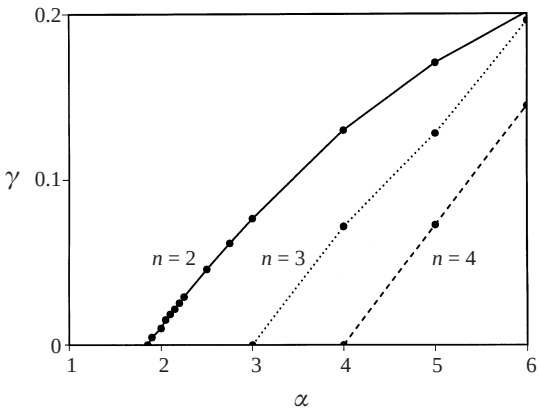

FIGURE 1. Growth rates γ for the barotropically unstable modes $n = 2, 3, 4$ versus the steepness parameter α.

This graph for the $n = 2$ mode is similar to that found by Carton & McWilliams (1989) except that they found anomalously high values of the growth rate for mode 2 near $\alpha = 2$. We believe the discrepancy is a matter of the resolution used in the determination of the stability. For azimuthal mode $n = 2$, we used numerical grids of both 64^2 and 128^2 points. At the lower resolution our results reproduced those in the Carton & McWilliams (1989) graph. The results shown in figure 1 for $n = 2$ are from the higher resolution calculation and these do not show the anomalously high growth rates obtained from the lower resolution calculation. For $n = 3$ and $n = 4$ the results presented are from the simulations with the 64^2 grid, which is adequate for current purposes.

From a given initial condition, the early evolution of the vortex is not necessarily dominated by the fastest growing mode for a given α. The early evolution may be a complicated combination of the evolution of many modes depending the initial amplitude of each mode. If the evolution were purely linear, then the mode with the largest growth rate would eventually dominate. In the actual evolution, however, nonlinear effects eventually cause the linear instability to cease or saturate. The resulting long-term evolution then can be highly dependent on the precise form of the initial condition. For example, for a high value of α (e.g. $\alpha = 6$), a random perturbation of the initial condition may eventually result in the formation of two dipole pairs or a stable quadrupole structure (cf. Carnevale & Kloosterziel 1994).

A particularly relevant set of two-dimensional numerical experiments consists of initializing the flow with a mode $n = 2$ perturbation to the basic profile. For α less than approximately 1.85 the vortex remains nearly circular and no instability is observed. For larger values of α up to about $\alpha = 3.25$, the outer annulus becomes unstable forming two satellites co-linear with the core. This is a stable tripole (cf. Legras, Santangelo, Benzi 1988; Carton *et al.* 1989; van Heijst *et al.* 1991; Kloosterziel & van Heijst 1991). For even larger values of α, although it appears that a tripole begins to form, this is only an intermediate state. The core is eventually sheared in two by the action of the satellites, and the whole structure breaks into a pair of stable dipoles propagating away from each other.

Thus if we could ignore the three-dimensional aspects of this problem, the outcome of a particular instability would depend on the nature of the initial perturbation and the size of α. In other words, save for direction of rotation, there would be no

difference in how cyclones and anticyclones evolve. The evolution would depend only on what unstable modes are initially excited and with what amplitudes. For example, if we excite a mode-2 perturbation on a basic profile with $\alpha = 3$, we would observe stable tripole formation for both cyclones and anticyclones. From the point view of two-dimensional theory, the asymmetry between cyclones and anticyclones could only be in the preparation of the initial condition.

In contrast to the purely two-dimensional barotropic instabilities, the centrifugal instability is inherently three-dimensional. Rayleigh investigated the centrifugal instability considering only axisymmetric motions. Under that condition, he showed that the flow is unstable if the gradient of the magnitude of the angular momentum is negative somewhere in the vortex. In a rotating flow, this criterion can be written in terms of the azimuthal velocity v_θ and vertical vorticity ω_z as (cf. Kloosterziel & Van Heijst 1991)

$$(v_\theta + r\Omega)(\omega_z + 2\Omega) < 0, \tag{2.8}$$

where Ω is the angular rotation rate of the environment. The left-hand side of inequality (2.8) is proportional to and has the same sign as a quantity traditionally called the Rayleigh discriminant. The inequality is a sufficient condition for linear instability due to three-dimensional overturning motions. It is strictly valid only in the case where motions are artificially restricted to being axisymmetric. Nevertheless, the inequality (2.8) has proven to be a reliable indicator of centrifugal instability in a variety of cases where this restriction is relaxed (cf. Smythe & Peltier 1994; Carnevale *et al.* 1997*a*).

By substituting the formulas for ω_z and v_θ from our basic profile into the criterion for instability, we obtain the following explicit criterion for this isolated vortex:

$$[\mathrm{e}^{-\rho^\alpha} + N][(1 - \tfrac{1}{2}\alpha\rho^\alpha)\mathrm{e}^{-\rho^\alpha} + N] < 0, \tag{2.9}$$

where, for given values of N and α, inequality (2.9) determines the values of r for which instability is possible. By examining the behaviour of the two factors in square brackets, we find that the instability criterion can only be satisfied for rotation numbers satisfying $-1 < N < N_{cr}$ where

$$N_{cr} = \tfrac{1}{2}\alpha \exp\left(-\frac{\alpha + 2}{\alpha}\right). \tag{2.10}$$

This is very different from the case of the single-signed, Gaussian vorticity profile, $\omega_z = \omega_0 \exp(-r^2/2\sigma^2)$, which is unstable only for sufficiently strong anticyclones (i.e. $-1 < N < 0$; cf. Carnevale *et al.* 1997*a* and references therein). For the isolated vortex case, even cyclones can be centrifugally unstable if the rotation number is sufficiently low (cf. Kloosterziel & van Heijst 1991). For sufficiently high rotation numbers, both cyclones and anticyclones will be centrifugally stable, and, for sufficiently high rotation number, both cyclones and anticyclones will behave similarly as noted in the introduction.

For a given rotation number and steepness such that the flow is unstable, the formula (2.9) also predicts the physical region of instability. This is shown in figure 2 where we plot both the inner and outer radii of the instability region, r_- and r_+, respectively, as functions of N for $\alpha = 2, 3$ and 5. For $N = 0$, the inner radius of the instability region coincides with $r_\times$, where the vorticity changes sign, and the outer radius of the instability region is infinite. As N increases or decreases toward the stability boundaries for any α, the radial extent of the instability region shrinks. For anticyclones the region of instability moves toward the centre of the vortex as

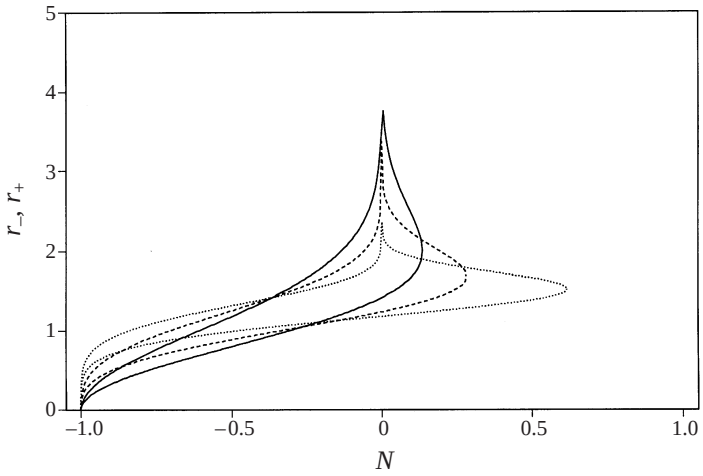

FIGURE 2. Radial positions where the sign of the left-hand side of equation (2.8) changes sign (———, $\alpha = 2$; – – – –, $\alpha = 3$; ·····, $\alpha = 5$).

$N \to -1$, while for cyclones the inner radius of the instability region increases as N increases. Thus, for cyclones the region of instability for the profile (2.1) is always outside the core of the vortex.

We can also examine formula (2.9) analytically in the vicinity of the values $N = -1, 0$ and N_{cr} to obtain approximate values $r_- < r_+$ for the limits on the region of instability. For $N = 0$ the value of r_+ diverges while $r_- = r_\times$. This is the case without rotation and we see that the vortex is centrifugally unstable except in the inner core of radius $r_- = r_\times$. Near $N = 0$ we can write

$$r_- \sim \sqrt{2}\sigma \left[\frac{2}{\alpha}(1 + N\mathrm{e}^{2/\alpha}\right]^{1/\alpha}, \tag{2.11}$$

while for r_+ the results differ depending on the sign of N. We have

$$r_+ \sim \sqrt{2\sigma}\left[-\ln\left(\frac{2N}{\alpha \ln(1/N)}\right)\right]^{1/\alpha} \quad \text{for} \quad N \gtrsim 0. \tag{2.12}$$

and

$$r_+ \sim \sqrt{2\sigma}[-\ln(-N)]^{1/\alpha} \quad \text{for} \quad N \lesssim 0. \tag{2.13}$$

For $N \gtrsim -1$ we have

$$r_- \sim \sqrt{2\sigma}\left[\frac{2}{2+\alpha}(1+N)\right]^{1/\alpha} \tag{2.14}$$

and

$$r_+ \sim \sqrt{2\sigma}[-\ln(-N)]^{1/\alpha}. \tag{2.15}$$

Finally, for $N \lesssim N_{cr}$ we have

$$r_\pm \sim \sqrt{2\sigma}\left[\frac{2+\alpha}{\alpha} \pm \left(2\left(1 - \frac{N}{N_{cr}}\right)\right)^{1/2}\right]^{1/\alpha}. \tag{2.16}$$

Although a complete analytical theory of the linear instability of isolated vortices in rotating flow is not available, we can try to combine the above ideas of two-dimensional or barotropic instability with centrifugal instability to attempt to

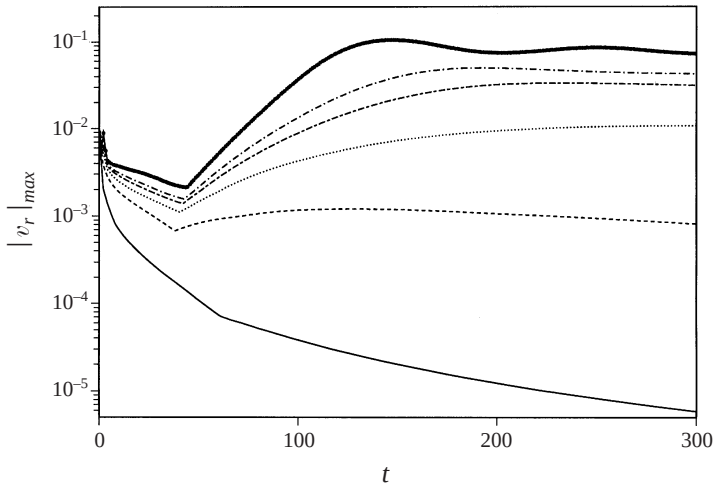

FIGURE 3. History of $|v_r|_{max}$ for two-dimensional simulations at different Reynolds numbers (———, $Re = 100$; – – – –, $Re = 400$; ·····, $Re = 700$; — – —, $Re = 1000$; — · —, $Re = 1250$; · · · ·, $Re = 2500$).

understand the wide variety of results on the evolution of isolated vortices obtained in the laboratory and numerical simulations.

3. Numerical simulations without Ekman effects

We have performed numerical simulations of the evolution of isolated vortices subject to three different kinds of boundary conditions. The simulations are performed with a finite difference code that solves the Navier–Stokes equations in cylindrical coordinates. The code is described in detail in Verzicco & Orlandi (1996). The versatility of the code has been demonstrated by application to several different physical cases. For example, it has been applied in the investigation of Taylor stratified flows by Hua, Le Gentil & Orlandi (1997), baroclinic and barotropic instabilities by Verzicco, Lalli & Campana (1997), natural convection in metals by Verzicco & Camussi (1997), and flow in rotating turbulent pipes by Orlandi & Fatica (1997). For our simulations, the axis of the cylindrical coordinates coincides with the axis of rotation. The boundary on the sidewalls is kept as free-slip in all of the simulations presented here. At the top and bottom of the domain, we have the option of choosing periodic, free-slip or no-slip conditions. Periodic boundary conditions are useful for testing the predictions based on two-dimensional results and the centrifugal instability theory discussed above. We will see that the results using slip boundary conditions on the top and bottom are very similar to the periodic boundary condition case. The most relevant choice of boundary conditions with regard to the laboratory experiments has a no-slip condition on the bottom boundary and a free-slip condition on the top boundary. As we shall see in §4, the presence of the no-slip bottom causes an Ekman layer to form on the bottom, and this greatly increases the complexity of the flow.

3.1. *Two-dimensional simulations*

Since the barotropic instability is an inviscid instability, it is important to know at what level of viscous dissipation the development of the instability will be arrested. To obtain some quantitative measure of the size of the Reynolds number below

which we would not expect to see the barotropic instability, we performed a series of two-dimensional simulations by running our three-dimensional code with only one grid point in the vertical. The initial axial vorticity $\omega_z(r)$ was perturbed by adding some noise to the scaled radius ρ. Specifically, in the formula (2.1), ρ is replaced by ρ^* given by

$$\rho^* = \rho + 0.25\eta \exp(-4(\alpha\rho^\alpha - 2)^2), \tag{3.1}$$

where $\eta(r, \theta, z)$ is a different random number for each point in the computational domain and is distributed between 0 and 1. The velocity field is then obtained by integration and application of the continuity equation. The exponential term in equation (3.1) causes the perturbation to have its maximum effect at the radial location where the main vorticity changes sign. Thus the perturbation involves both part of the core and part of the outer annulus. For example, with $\alpha = 3$, the perturbation to ρ peaks at $r_\times \approx 1.2$ and falls to the 10% level at $r \approx 1$ and $r \approx 1.4$. In previous studies, perturbing near the boundary between the core and the annulus was found useful in exciting the barotropic instabilities observed in the lab (cf. Carnevale & Kloosterziel 1994; Orlandi & van Heijst 1992), and so we have adopted this method here as well.

Note that with this disturbance, typically, no single azimuthal mode dominates (in contrast to the disturbances imposed by Carnevale & Kloosterziel 1994 who investigated the effects of preferentially exciting specific azimuthal modes). The r.m.s. amplitude of η here is set equal to 0.025. For the periodic boundary condition simulations that we discuss, the value of α was 3. According to figure 1, the most unstable mode is then $n = 2$ and a tripole is expected to form. As a measure of deviation from the circularly symmetric state, we can use the radial velocity v_r, which would remain zero if the vortex remained circularly symmetric. From the evolution of the maximum of v_r we can determine the Reynolds number at which the azimuthal instability can occur in spite of the presence of viscosity. Figure 3 shows that, as expected, the random perturbation initially decays to select the most unstable mode. In other words, there are many components of the initial perturbation that are not unstable, and these decay producing in the early evolution a net decay of the maximum v_r. Meanwhile the unstable modes grow and eventually dominate the signal if they are not first overcome by viscous effects. Thus, depending on the value of *Re*, the maximum v_r will either continue to decay from its initial value or begin to grow at a certain point due to the barotropic instability. In the long run, viscous effects will cause the signal to eventually decay as all motion must decay away. From these simulations, we found that for $Re < 500$ tripole formation is suppressed. For such low Reynolds numbers, only weak side lobes form during the evolution and the structure remains nearly circularly symmetric. For $Re > 1000$, strong tripoles emerge with well-defined side lobes, and, therefore, in this regime, horizontal diffusion due to viscosity should play little role in suppressing the two-dimensional instabilities. All of the three-dimensional simulations that we discuss below were performed with an initial Reynolds number of 2500, which is in the range typically found in the laboratory experiments discussed above.

3.2. *Three-dimensional simulations with periodic boundary conditions*

Three-dimensional simulations in which the boundary conditions in the z-direction are periodic allow us to look at the combined effects of the centrifugal instability and the barotropic instability without including complications of the bottom boundary layer. We will reserve the discussion of the effects of the viscous boundary layer for the next section.

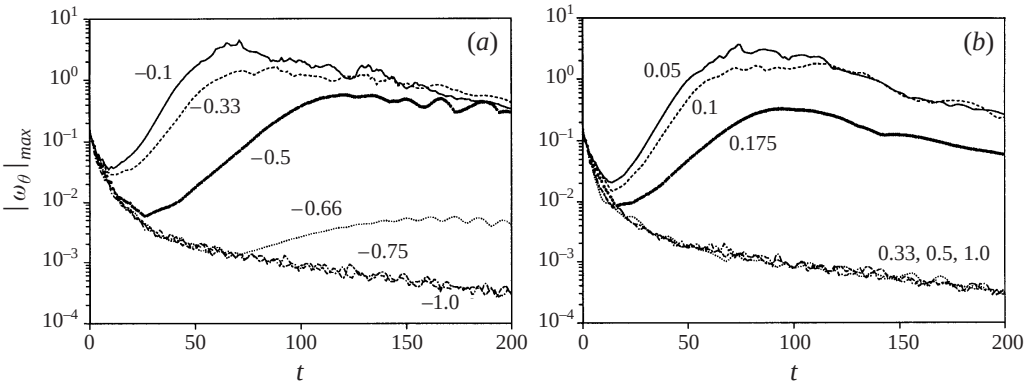

FIGURE 4. History of $|\omega_\theta|_{max}$ for three-dimensional simulations with periodicity in z for (a) anticyclones (———, $N = -0.1$; – – – –, $N = -\frac{1}{3}$; • • •, $N = -0.5$; ·····, $N = -0.66$; — – —, $N = -0.75$; — · —, $N = -1.0$); (b) cyclones (———, $N = 0.05$; – – – –, $N = 0.1$; • • •, $N = 0.175$; ·····, $N = \frac{1}{3}$; — – —, $N = 0.5$; — · —, $N = 1.0$). The values of N for each curve are also indicated in the figures.

To see whether the three-dimensional simulations capture the stability limit for centrifugal instability, we have performed a series of simulations with N ranging in value from -2 to $+2$ with the initial profile corresponding to $\alpha = 3$. If present, centrifugal instability should amplify our initial three-dimensional perturbation. As a measure of the three-dimensional overturning motions, we have plotted in figure 4, the maximum of $|\omega_\theta|$ as a function of time. In figures 4(a) and 4(b), we see the results for the anticyclones and cyclones respectively. Each graph shows how the maximum $|\omega_\theta|$ evolves in time for different values of N. Let us consider the anticyclonic case (figure 4 a) first. Centrifugal instability is predicted for all values of N in the range $(-1, 0)$. In all cases shown on the graph, the maximum value of $|\omega_\theta|$ decreases initially. If there are growing modes, then their contribution to $|\omega_\theta|_{max}$ will eventually dominate over the contribution of the decaying modes. This appears to happen in the cases with $N = -\frac{1}{10}, -\frac{1}{3}, -\frac{1}{2}$, and $-\frac{2}{3}$. We also note that after a period of exponential growth, there is a long slow decay which is due to viscous decay. The unexpected result is that there seems to be no period of exponential growth for the case $N = -0.75$. We see that as N increases, the time of onset of the growth of $|\omega_\theta|_{max}$ increases and the maximum value of $|\omega_\theta|_{max}$ that is achieved decreases. Thus it may be that the instability corresponding to $N = -0.75$ will only be evident after a time $t = 200$. On the other hand, it may be that for this N the centrifugal instability is damped and prevented from occurring by viscous decay. Also we can note from figure 2 that as one moves from $N = 0$ toward $N = -1$, the radial width of the instability regime shrinks and the centre of the regime moves toward the centre of the vortex. Since the initial perturbation is concentrated near the boundary between the vortex and the core, this means that the perturbation will be less effective in initiating the instability as $N \to -1$.

Turning next to the cyclonic case, we see a period of exponential growth for the cases $N = 0.05, 0.10$ and 0.175. While for $N \geqslant 0.33$, there is just decay. This is in accord with the critical value of N being 0.28 for the cyclones with $\alpha = 3$ (see equation (2.10)).

To better understand the nature of the centrifugal instability, we can plot contours of ω_θ in a vertical (r, z) cross-section for a given angle θ. Here we choose θ such that the cross-sectional plane passes through the point where ω_z takes its most negative

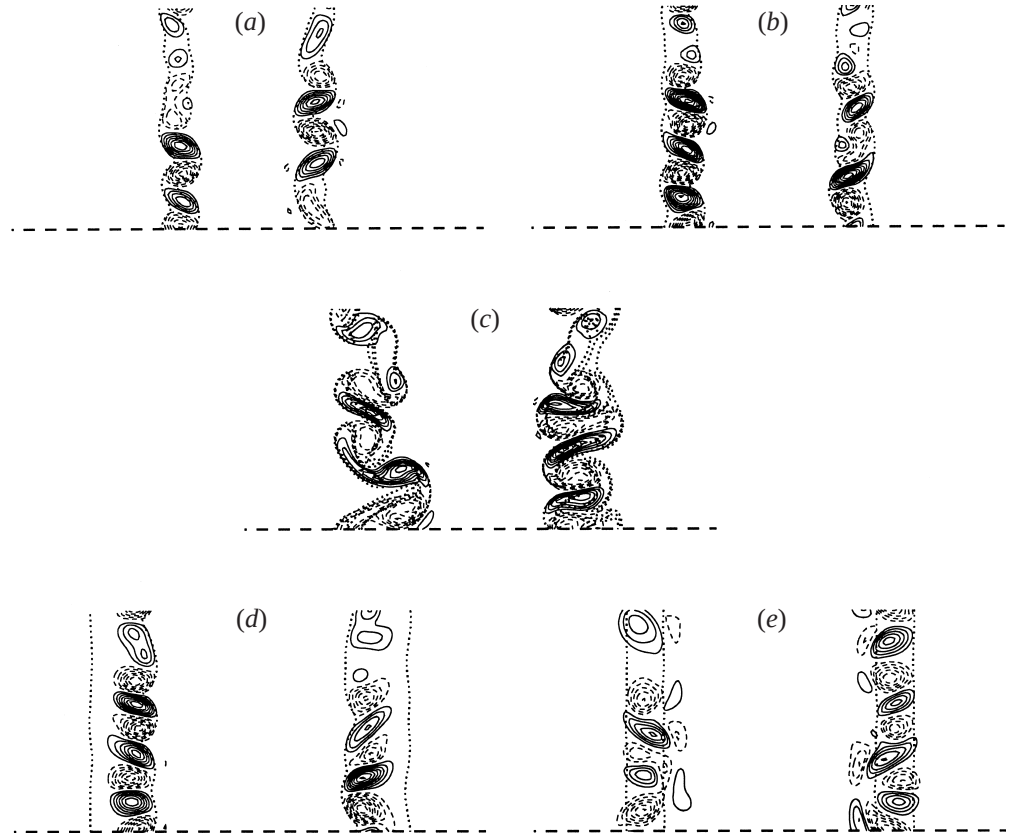

FIGURE 5. Contours of ω_θ in vertical sections that pass through the point where ω_z takes its lowest value. (*a*) $N = -0.5$, $t = 100$, (*b*) $N = -1/3$, $t = 50$, (*c*) $N = -0.1$, $t = 50$, (*d*) $N = +0.1$, $t = 50$, (*e*) $N = +0.175$, $t = 100$; ———, $\omega_\theta > 0$; – – – –, $\omega_\theta < 0$ (*a,b,d,e*: contour level increment $\Delta\omega_\theta = 0.05$); (*c*: $\Delta\omega_\theta = 0.2$). The dotted lines are those where the left-hand side of inequality (2.8) vanishes. The dashed line simply indicates one end of the computational domain.

value. Such cross-sections are shown in figure 5 for a representative sample of the centrifugally unstable cases. In addition to the contour levels of ω_θ, we have also indicated with dotted lines the region where the Rayleigh discriminant is negative (see equation (2.8)). For axially symmetric flows, it is in this region that linear theory allows instability. During the nonlinear evolution of the vortex, this region is distorted from the initial axially symmetric annulus and the Rayleigh criterion can no longer be expected to define the region of instability perfectly. Nevertheless, even at the relatively late times shown, we see that the most intense three-dimensional activity does occur within the region of the negative Rayleigh discriminant. Note that in the $N = 0.10$ case, we see that the instability seems to be mainly near the inner edge of the negative Rayleigh discriminant region. This recalls the finding for non-isolated vortices (Carnevale *et al.* 1997*a*) that the centrifugal instability begins near the inner edge of the instability region and spreads out from there.

The early form of the instability appears to involve the formation of a series of coaxial vortex rings that encircle the core of the primary vortex. The values of ω_θ in these rings alternate in sign as one goes from one ring to the next in the vertical direction. These vortical structures are reminiscent of the 'rib' vortices in mixing layers, where they tend to be generated in the region of maximum shear. The vortex tilting

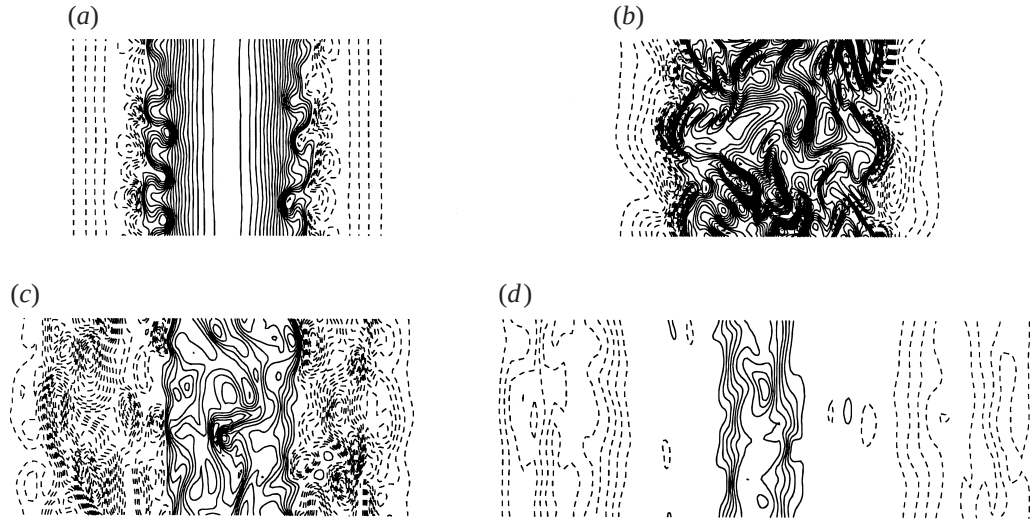

FIGURE 6. Contours of ω_z in vertical sections that pass through the point where ω_z takes its most negative value (*a*) $t = 50$, (*b*) $t = 100$, (*c*) $t = 150$, and (*d*) $t = 200$ ($N = -1/3$, $\alpha = 3$; $\Delta\omega_z = 0.05$; ———, positive values; – – – –, negative).

term in the vorticity equations is responsible for the generation of such structures (Cantwell 1981; Libby 1996).

An important effect of the centrifugal instability is the steepening of vorticity gradients. This appears to be due to the advection of fluid by the 'rib' vortices. The effect can be understood by considering the flow around any pair of counter-rotating vortices. Between such a pair of rib vortices fluid is advected either toward or away from the core, depending on whether the vortex on top of the given pair has positive or negative ω_θ. For example, consider a pair of adjacent rib vortices that form rings around the axial core of the primary vertically-aligned vortex. If the upper/lower rib vortex has positive/negative ω_θ, then in between the two rib vortices there is a flow toward the core of the primary vortex. Furthermore, in the region on the side of the rib vortices closest to the axis of the primary vortex, there is an induced relative flow that locally tends to stretch and so enhance the vertical vorticity of the primary vortex. If we consider a rib vortex pair with the upper/lower vortex having negative/positive ω_θ, then it is the side of the vortices farthest from the axis of the primary vortex where stretching of the vertical vorticity of the primary vortex is induced. This creates regions of greatly enhanced vorticity gradients.

An example of the effect of vortex stretching by the rib vortices can be seen in figure 6(*a*) (representing time $t = 50$), which shows a contour plot of ω_z in vertical cross-section for the case $N = -\frac{1}{3}$. By measuring the radial profile of v_θ averaged over θ and z, we have found that the profile has become steeper than the critical $\alpha = 3.25$ profile, which is the profile that divides the regime of tripole formation into a region of stable tripole formation and unstable tripole formation based on pure two-dimensional evolution. Hence, this steepening of gradients can trigger the formation of an unstable tripole. By time $t = 100$ (figure 6*b*), the variability in ω_z has spread both toward and away from the centre of the vortex, penetrating well within the core of the vortex. Even at this time the enhancement of vorticity gradients in front of advancing ring pairs is still visible; however, as we can see from figure 4(*a*), decay of the three-dimensionality of the structure has begun. Then the three-dimensional variability

in the ω_z field decreases with the vorticity field becoming increasingly columnar. The barotropic instability that the structure undergoes produces an unstable tripolar structure, whose cores can be seen in figure 6(*d*), but it is easier to see this in a horizontal cross-section which we shall turn to now.

In figure 7(*c*), we see the evolution of the tripolar structure, for $N = -\frac{1}{3}$, in horizontal cross-sections of the ω_z field. At $t = 100$ the gradient of vorticity has become relatively strong in a narrow band. By $t = 150$, there is the formation of a transitory quadrupole state which typically occurs only for profiles significantly steeper than the $\alpha = 3$ profile, so that at least azimuthal modes $n = 2$ and $n = 3$ are unstable as we saw in figure 1 (cf. Orlandi & van Heijst 1992; Carnevale & Kloosterziel 1994). In two-dimensional simulations, a symmetric form of the quadrupole seems to be stable to sufficiently small perturbations (Carnevale & Kloosterziel 1994), but in the laboratory or in these three-dimensional simulations, the quadrupole has been observed only as an unstable intermediate state. Also, as observed in the laboratory and two-dimensional simulations, this intermediate state becomes a tripole by the merger of two of the cyclonic satellites. This is the tripole that was shown in vertical cross-section in figure 6(*d*). This tripole is unstable. The instability proceeds by the shearing apart of the core anticyclonic vortex by the two cyclonic satellites. The anticyclone then rolls up into two vortices that pair with the satellites forming the two dipoles that propagate away from each other as shown in figure 8, which corresponds to time $t = 400$. This is the 'double-dipole' instability that occurs for a pure barotropic mode 2 instability with $\alpha > 3.25$.

An example of the double-dipole instability for a centrifugally unstable anticyclone is shown in Kloosterziel & van Heijst (1991). Much of the three-dimensional visualization of the instability of vortices in a rotating tank has been accomplished by recording the images of a distribution of dye that is initially concentrated where the vortex is created. Numerically, it is difficult to follow the details of the dye distributions as used in the laboratory because the diffusivity of dye is very small – the diffusivity of typical dyes is three orders of magnitude smaller than kinetic viscosity in water. The small diffusivity means that the flow field can create filaments of dye much finer than those of the more rapidly diffusing vorticity. When the thickness of such filaments becomes comparable to the grid size of the computational domain, the simulation is no longer valid. To avoid this problem we are forced to use a passive tracer diffusivity that is much larger than the corresponding dye diffusivity. Nevertheless, our simulations of passive tracer evolution do capture many of the features of the evolution of the dye field as observed in the laboratory, at least for the short time scales relevant here. An example of this is shown in figure 8, where, in addition to isovortical contours of the vorticity field, we have also shown isoconcentration lines of a field of passive tracer that was simulated along with the evolution of the vorticity field. The initial passive tracer was distributed with intensity proportional to the magnitude of the initial vorticity field. Even though we set the passive scalar diffusivity equal to that of the viscosity, the tracer pattern in figure 8 is similar to the dye results observed in the laboratory for this instability, and, in particular, we note the typically observed filament of dye curved around the front of each of the propagating dipoles.

In figure 7, we have also plotted the evolution of ω_z in horizontal cross-section for other values of N illustrating a transition for anticyclones from barotropic stable tripole formation to complete destruction of the vortex by centrifugal instability. The cross-sections are shown for times $t = 100, 150$ and 200. We have not shown the case $N = 0$ (i.e. no rotation) because at the Reynolds number that we are

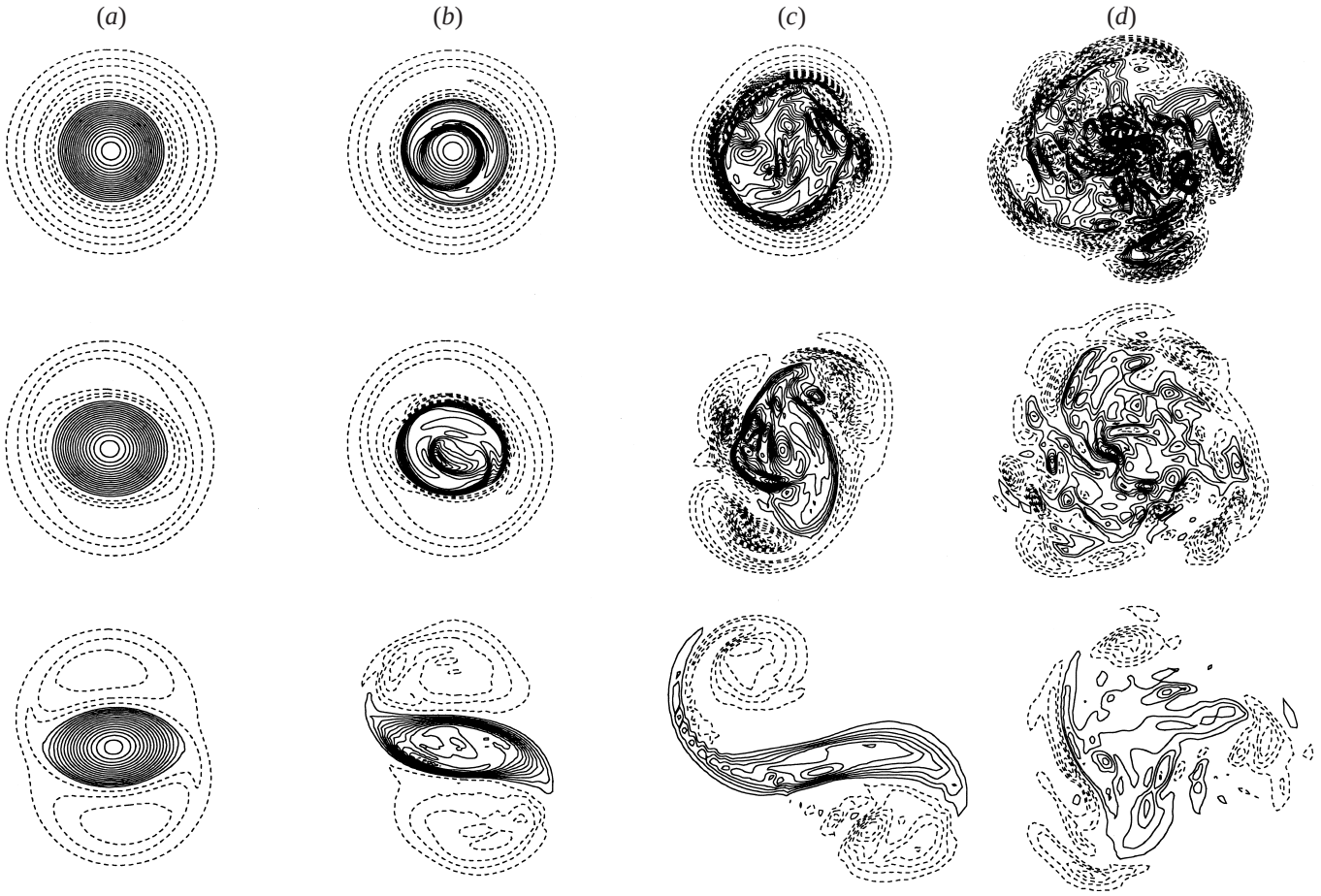

FIGURE 7. Contours of ω_z on horizontal planes at mid-height ($\Delta\omega_z = 0.05$). From left to right (*a*) $N = -2/3$, (*b*) $N = -1/2$, (*c*) $N = -1/3$, (*d*) $N = -1/10$. From top to bottom $t = 100$, $t = 150$, $t = 200$ ($\alpha = 3$).

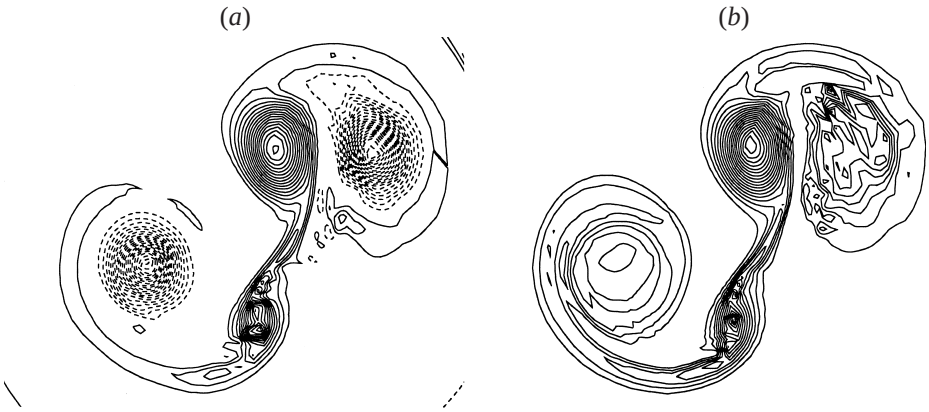

FIGURE 8. Double-dipole formation for $N = -1/3$ with $\alpha = 3$ at $t = 400$. (*a*) Contour levels of ω_z with $\Delta\omega_z = 0.01$; (*b*) isolines of passive scalar concentration.

using here, we did not have sufficient resolution to follow the evolution of that case, which generates very small scales of motion, beyond time $t = 50$. The eventual outcome of centrifugal instability in that case will be isotropic three-dimensional turbulence. All of the anticyclones illustrated in figure 7, should be unstable to three-dimensional overturning motions according to the instability criterion ($-1 < N \leqslant 0$) for centrifugal instability discussed above. In figure 7(*a*) ($N = -0.67$) is an example of the two-dimensional or barotropic instability that saturates in the form of a tripole. There is no evidence of any effects from small-scale three-dimensional motions even though there is a period of growth of such motion as indicated in figure 4(*a*), since the amplitudes of the three-dimensional motions always remain insignificant, with $|\omega_\theta|_{max}$ never rising above its initial value. The case $N = -0.50$ (figure 7*b*) shows some small-scale variability and an enhancement of the vorticity gradient between the core and the annulus, which as we suggested before is probably due to the advection by the 'rib' vortices. The steepening of the profile here was not sufficient to disrupt the formation of the tripole, which appears stable at time $t = 200$. By decreasing the magnitude of N further, we can increase the effect of the centrifugal instability as is suggested by figure 7(*c*) for the case $N = -\frac{1}{3}$. In this case, by time $t = 100$, there has been substantial steepening of the vorticity gradients as we discussed above. Next, in figure 7(*d*), we have an example at $N = -0.10$ in which the centrifugal instability is so vigorous that the coherent part of any simple barotropic instability is completely obscured. Note that the instability completely engulfs the core of the vortex.

We turn now to figure 9 with the results from the simulations of the evolution of the cyclones. We expect centrifugal instability for $0 < N < N_{cr}$ where, for $\alpha = 3$, $N_{cr} \approx 0.28$ (see (2.10)). In figure 9(*a*), showing the evolution for $N = 0.10$, the effect of the centrifugal instability shows up most strongly in the disruption of the negative-vorticity annulus. Figure 2 demonstrates that as the value of N increases the region of instability becomes narrower and shifts away from the core. From formula (2.3), it follows that the vorticity in our profile changes sign at $r \approx 1.2\sigma$; for $\alpha = 3$ and $N = 0.1$, we can deduce from figure 2, or from the approximate formula (2.11), that the instability regime will start at a radius beyond this value. Thus the instability band in this case is entirely contained in the outer annulus, and this is verified by the simulation shown in figure 9(*a*). The disruption and subsequent diffusion of the annulus of negative vorticity by centrifugal instability results in a stable monopolar

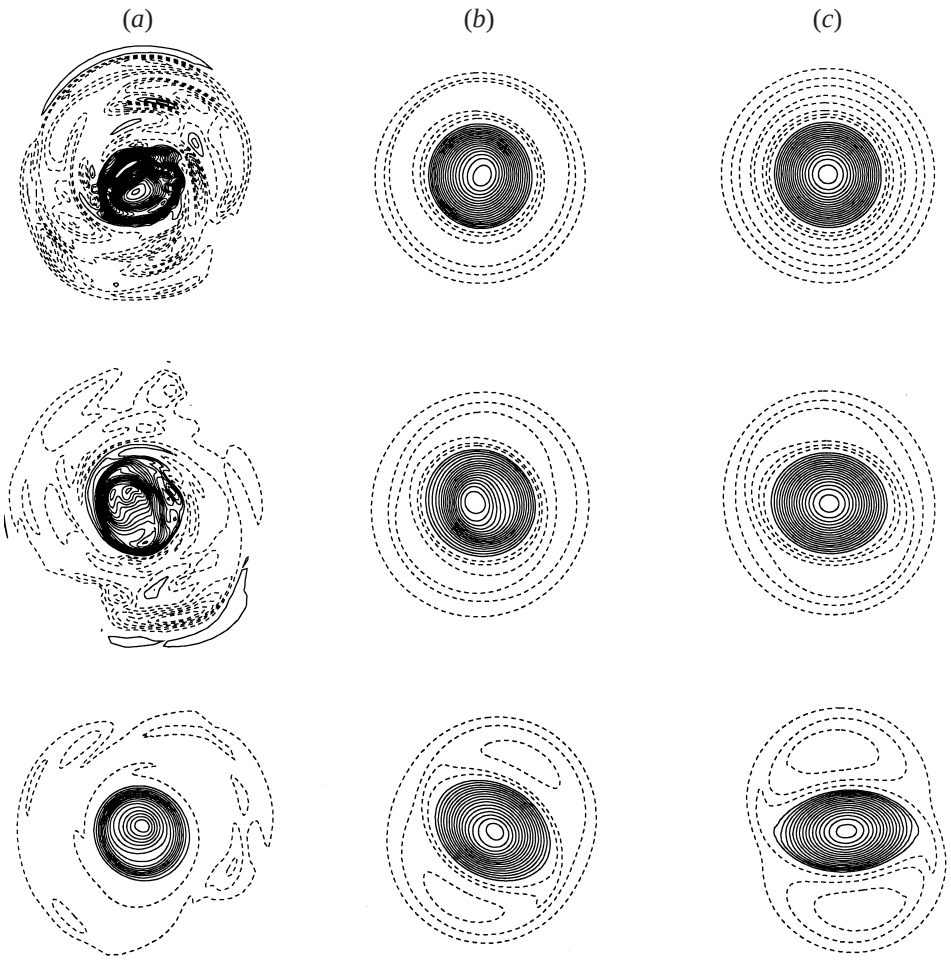

FIGURE 9. Contours of ω_z on mid-height planes ($\Delta\omega_z = 0.05$); (*a*) $N = +1/10$, (*b*) $N = +0.175$, (*c*) $N = +1/3$. From top to bottom $t = 100$, $t = 150$, $t = 200$ ($\alpha = 3$).

vortex. This is in strong contrast to the effect of the centrifugal instability for the anticyclones, where we found the rib vortices enhanced the vorticity gradients. It is also very different from the anticyclonic case at $N = -0.1$ where we saw the complete disruption of the annulus and the core. Here for $N = 0.1$ the core is well preserved. The rib vortices do not penetrate into the core, and the centrifugal instability tends to make the vortex profile shallower. Comparison with the ideal profile (2.1) shows that the structure is distorted so that an α value cannot be defined. The profile near the core is somewhat steeper than that for the core at $\alpha = 1.85$, but, the rest of the profile is broader. For a model of an isolated vortex composed of two circular patches of uniform vorticity, the vortex becomes stable if the width of the outer annulus is sufficiently broad (cf. Flierl 1988; Kloosterziel & Carnevale 1992). The prediction for the two-patch system is that the vortex is stable if $d/a > (1 + \sqrt{2})^{1/2}$ where d is the radius of the outer patch and a is the radius of the inner patch. This can also be restated in terms of the jump in vorticity from the core to the anulus. Stability requires $(\omega_0 - \omega_1)/\omega_0 < 1 + 1/\sqrt{2}$. Thus if the annulus is broad enough or, equivalently for the two-patch system, if the vorticity amplitude in the annulus is sufficiently small, then

the structure is stable. The vorticity distribution shown in figure 9(*a*) is somewhere between a two-patch vortex and the continuous profile defined by α. Unfortunately, there is no simple criterion that we can give for stability in terms of any obvious measure of the overall steepness of the profile. In particular, there does not appear to be any simple way to relate α with d/a for the two-patch system.

In figure 9(*b*), we show the result for the case with $N = 0.175$, which is in the regime predicted to be centrifugally unstable by the Rayleigh criterion. In figure 4(*b*), we saw evidence that the centrifugal instability does indeed occur for this value of N. However, that figure also shows that the strength of the instability is very limited, with $|\omega_\theta|_{max}$ never reaching more than three times its initial value. Given that the initial perturbation is very weak, it seems that the instability is arrested by the presence of viscosity and does not disrupt the vortex, which evolves like a two-dimensional structure to form a tripole. Increasing N to $\frac{1}{3}$, we observe essentially the same behaviour as that for the anticyclone shown previously in figure 7(*a*), corresponding to $N = -\frac{2}{3}$. Both the $N = \frac{1}{3}$ and the $N = -\frac{2}{3}$ cases show the formation of very symmetric and stable tripoles. As $|N|$ is increased further from these values, the flows for cyclone and anticyclone look more and more similar (we have tested up to $|N| = 2$), in accord with the Taylor–Proudman theorem.

An important point can be made concerning the difference between the tripole formation and the double-dipole instability. Compare figures 7(*a*) and 7(*c*) for the evolution of the tripole at $N = -\frac{2}{3}$ and for the double-dipole instability at $N = -\frac{1}{3}$. At time $t = 200$, we note that although both positive and negative relative vorticity amplitudes have decayed in both cases over the course of the simulation, the relative decay in the core and satellites is very different in the centrifugally stable and unstable cases. In the case that produced the tripole, the magnitude of vorticity in the satellites has fallen to about 1/8 that in the core – Kloosterziel & van Heijst (1991) say on page 9 that 'the amplitudes of the vorticity of the core and the satellites differ by at least a factor of 5 shortly after they have formed', which is in accord with our simulations. In the vortex which evolves according to a double-dipole instability, the magnitudes of vorticity in the core and the satellites are roughly the same. Since in the initial condition (with an $\alpha = 3$ profile), the ratio of vorticity magnitude in the annulus to that in the core is about 1/6, it appears that in this case the centrifugal instability acts to greatly enhance the magnitude of the negative relative vorticity, that is the vorticity of the annulus, compared to the positive relative vorticity of the core. This is a significant finding, because it means that these differences in relative vorticity magnitudes can be produced entirely by centrifugal instability, and do not require nonlinear Ekman effects as was previously thought.

At this point, we have seen that centrifugal instability alone can steepen an anticyclonic profile and initiate the double-dipole instability. Thus it is tempting to consider this the mechanism responsible for the difficulty of producing anticyclones in the laboratory. However, if centrifugal instability were the only mechanism inhibiting the formation of stable anticyclonic tripoles, it should be possible to produce them if N is sufficiently high. In fact recently such a tripole has been successfully created by Satijn & van Heijst (personal communication, 1998). On the other hand, Kloosterziel & van Heijst (1991) noting the difficulty in producing a stable anticyclonic vortex even for relatively high N suggested that the dynamics of the Ekman layer may play a role in inhibiting the formation of stable tripoles from anticyclones. This is a point we will return to later.

We will end this section with a summary of its main results. We were able to produce numerically the full evolution of an unstable vortex including the centrifugal

instability, the triggering of the barotropic instability by the centrifugal instability, the production of a multipolar state and the simultaneous relaxation to columnar structures for all of the vortices (e.g. see figure 15*c*). In a series of simulations with different values of N, we found that the flows did exhibit centrifugal instability in a range approximating that predicted by inviscid theory ($-1 < N < N_{cr}$), but the instability was clearly inhibited for $N \lesssim -0.75$, probably due to viscous effects. We found that the centrifugal instability involved the formation of 'rib' vortices that enhanced axial vorticity gradients. In the anticyclonic case, the centrifugal instability steepens the gradient of vorticity between the core and annulus of the primary vortex, and so encourages double-dipole and other instabilities of higher azimuthal mode number, whereas for the cyclone, the centrifugal instability effect occurs further away from the core and so cannot promote the high-order instabilities efficiently. In fact, for cyclones we have presented some evidence that the centrifugal instability may even broaden the annulus of opposite signed vorticity, which would be a stabilizing effect. Of all the effects that break the symmetry between cyclones and anticyclones in the laboratory experiments, this centrifugal instability may be the most important.

4. Three-dimensional simulations with no-slip boundary conditions

An important aspect of the laboratory experiments that has not been dealt with by the periodic boundary condition simulations discussed above is the presence of the bottom boundary of the tank. This boundary causes the formation of a bottom boundary layer, an Ekman layer, which will significantly enhance the rate of decay of the vortices (cf. Pedlosky 1979). Also, we might expect that any inertial wave radiation emanating from the vortex will be damped more rapidly in the presence of a no-slip wall because reflection from such a wall would produce large gradients of vorticity on which viscosity would act more effectively (cf. Greenspan 1980).

As a preliminary investigation of the effects of the bottom boundary, we performed a series of simulations with $\alpha = 3$, replacing the top boundary layer in the simulation with a free-slip condition. In one set of simulations we replaced the bottom boundary with a free-slip boundary and in another with a no-slip boundary. Figure 10 shows a comparison at time $t = 200$ of the vorticity fields for simulations in the case $N = -0.5$, all starting with the same initial condition, but having different boundary conditions. The result in the case where the boundaries on top and bottom are both free slip (10*b*) is very similar to the case with periodic boundary conditions (10*a*). More generally we find that although the change from periodic boundaries to free slip may change some of the timing of the evolution, there is not much qualitative change.

Figure 10 also shows that compared with the periodic boundary condition case, there is considerably more damping of the field in the no-slip case, and indeed the anticyclonic vortex shown in figure 10(*c*) does not reach the tripolar state. It appears that in this case, and for all $N < -0.5$, the barotropic instability is arrested by the damping effect of the bottom Ekman layer. In contrast, under the same conditions ($|N| = 0.5, \alpha = 3$), the cyclonic vortex does form a tripole with the no-slip boundary, as in the periodic boundary condition case. For the cyclones, even with the bottom Ekman layer, the sequence of predictions from two-dimensional barotropic instability studies seem to hold approximately. In other words, as the α of the initial condition is increased, there is a sequence of final structures that goes from stable monopole to stable tripole to unstable tripole. This is illustrated in in figure 11, where we show the results at $t = 200$ for $\alpha = 2$, 3 and 3.5 (with $N = \frac{1}{3}$). Although the two-dimensional inviscid studies predict the transition between monopole and stable tripole should

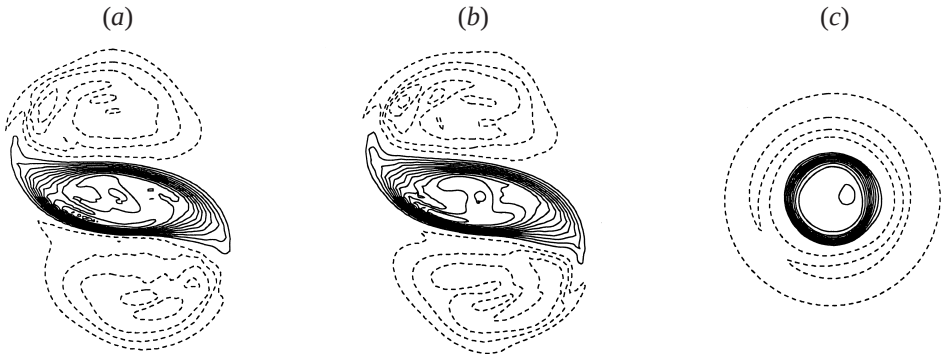

FIGURE 10. Contours of ω_z on mid-height planes ($\Delta\omega_z = 0.025$) for $N = -1/2$ at $t = 200$ for different boundary conditions along the vertical direction: (*a*) periodic, (*b*) free slip, (*c*) no slip ($\alpha = 3$).

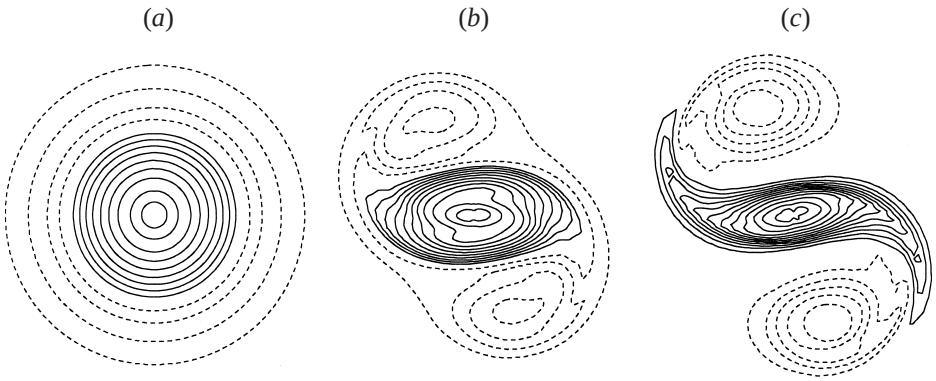

FIGURE 11. Contours of ω_z on mid-height planes ($\Delta\omega_z = 0.025$) for $N = 1/3$ at $t = 200$ with a no-slip bottom boundary condition. (*a*) $\alpha = 2$, (*b*) $\alpha = 3$, (*c*) $\alpha = 3.5$.

occur around $\alpha = 1.85$, the transition occurs at a somewhat higher α in the three-dimensional simulations with viscosity. We should also note that for $\alpha = 3.5$, the critical value of N for centrifugal instability is 0.36; however, as in the periodic boundary condition case, there seems to be little effect of centrifugal overturning on the evolution of the barotropic modes when N is close to the stability boundary. In figure 12 we will see another example of the formation of an unstable cyclonic tripole, but for a centrifugally stable value of N.

In order to understand better the difference between the effect of the bottom boundary in the anticyclonic case and the cyclonic case, we performed a series of simulations with $\alpha = 3.5$, in which case the barotropic instability is not completely damped for $N \leqslant -0.5$. Four representative cases are shown in figure 12. We have included two cases with high values of $|N|$ (i.e. $N = \pm 2$), which will be of use below in discussing the currently available theory of nonlinear Ekman layers, which holds only for large N.

In figure 12(*c*), we see the formation of an unstable tripole at $N = 0.5$. This N is certainly in the centrifugally stable range since for $\alpha = 3.5$ we have from equation (2.10) that $N_{cr} = 0.36$. Thus in this case, we have an example of the formation of an unstable cyclonic tripole without the effect of centrifugal instability. In the laboratory experiments discussed above, unstable cyclones usually evolved

into stable tripoles; however, van Heijst *et al.* (1991) show an example of a cyclone that does become an unstable tripole which then undergoes double-dipole instability. To explain the difference between this case of unstable cyclonic tripole formation and the usual stable cyclonic tripole formation, van Heijst *et al.* (1991) pointed out that the scatter plot of ψ vs. ω in the core of the cyclonic vortex in this case was different from that in the more typical case of the stable tripole. They suggested that it was the anomalous structure of the core itself that led to the unstable tripole formation. In contrast, our example in figure 12(*c*) requires nothing other than initially having a sufficiently high value of α for the formation of an unstable tripole.

For higher values of N, the damping effect of the Ekman layer becomes very important. At $N = 2$, we see that by $t = 200$ the amplitudes of both the positive and negative vorticity have decreased considerably more than in the lower N cases. A measure of the decay rate of vortices due to the Ekman layer is the Ekman time scale given by equation (2.7), which can be rewritten in terms of the advective time scale as

$$t_E/t_a = \frac{\sigma}{D}\left(\frac{2Re}{N}\right)^{1/2}. \tag{4.1}$$

For these experiments, our aspect ratio σ/D is $1/\pi$ and $Re = 2500$. Thus the final time shown in the figure $t = 200$ corresponds to $0.64t_E$ for $N = 0.5$ but $1.3t_E$ for $N = 2$. Thus it is natural to see considerably more damping the larger the values of N. Also, since the time scale of the barotropic or two-dimensional instability is controlled by the advective time scale, it is possible for a rapid Ekman decay to arrest the barotropic instability. In the $N = 2$ (figure 12*d*) example, a tripolar structure barely forms by $t = 200$, and although somewhat asymmetrical, it seems to decay as a weak tripole – we followed its evolution up to $t = 250$.

In figure 12(*b*) ($N = -\frac{1}{3}$), we have a typical double-dipole instability initiated by the centrifugal instability. In figure 12(*a*), we see the formation of a weak but symmetrical tripole for $N = -2$. Since this is initially an $\alpha = 3.5$ structure, we need to understand why it seems to follow a symmetrical tripole formation route rather than the unstable tripole to double-dipole route. Also since $|N| = 2$ represents a relatively high rotation rate, and centrifugal instability plays no role here, we need to understand why the evolution of the $N = -2$ is different from the $N = +2$ case since in pure two-dimensional theory the evolutions would be identical. Here we can have recourse to the theory developed for the nonlinear Ekman effect for axially symmetric vortices. If the equations of evolution are expanded for large N, the lowest order approximation is the linear Ekman decay, which can be expressed as a simple Newtonian damping in the equations of motion (cf. Pedlosky 1979), and which is the form that appears in quasi-geostrophic theory. The mechanism which produces the damping is that the boundary layer on the bottom no-slip surface gives rise to a secondary (i.e. first order in $1/N$) circulation, which includes a weak upward/downward flow at the bottom wherever the z-vorticity is positive/negative. This results in a compressing/stretching of the vortex column with a consequent reduction of the magnitude of the vorticity. This result is valid for sufficiently high N, while for finite N there are corrections to the simple linear decay law. Wedemeyer (1964) provides a theory for the next order correction in $1/N$ to the simple linear decay. A version of this theory for the evolution of isolated vortices is given in Kloosterziel & van Heijst (1992) and Maas (1993). The prediction is that v_θ, the azimuthal velocity field of the vortex, will decay

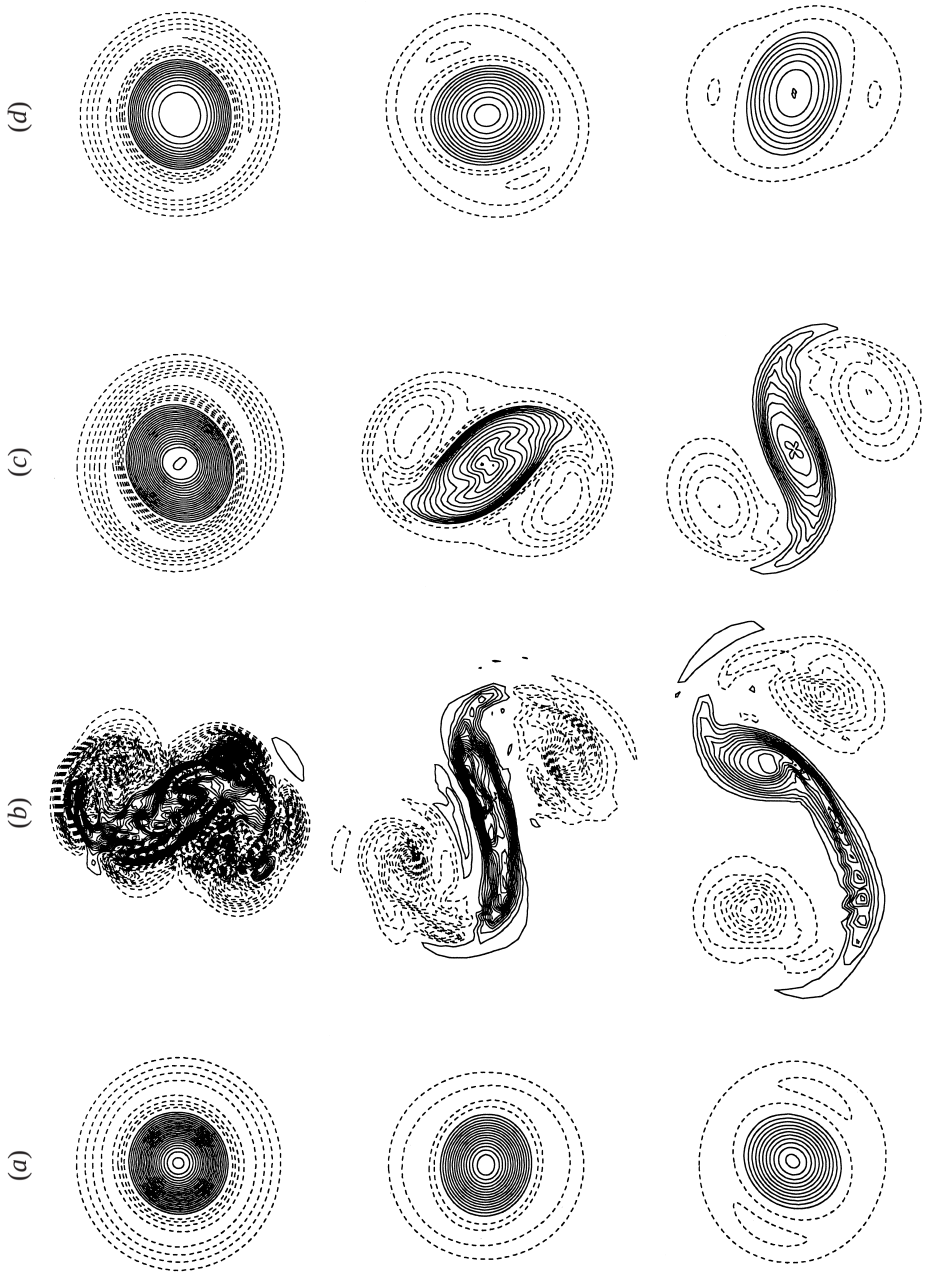

FIGURE 12. Contours of ω_z on mid-height planes from simulations with the no-slip condition at the bottom boundary ($\Delta\omega_z = 0.025$). From left to right (*a*) $N = -2$, (*b*) $N = -1/3$, (*c*) $N = 1/2$, (*d*) $N = 2$; from top to bottom $t = 100$, $t = 150$, $t = 200$.

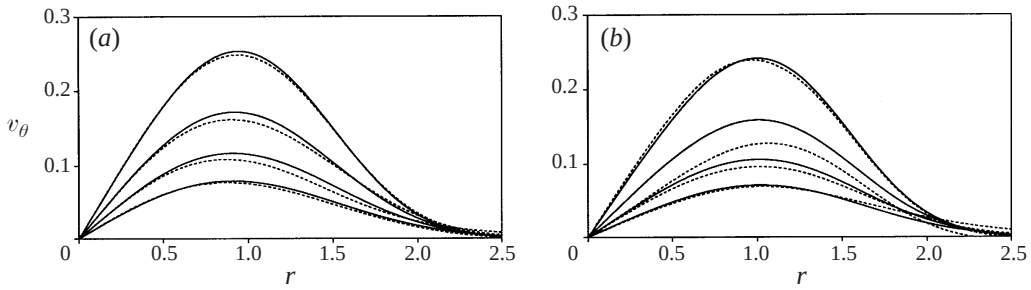

FIGURE 13. Velocity profiles for times $t = 50, 100, 150, 200$: ———, theory; – – – –, simulations at $\alpha = 3.5$ for (*a*) $N = -2$, (*b*) $N = 2$.

according to

$$\frac{\partial v_\theta}{\partial t} = -(1 + \omega_z/N)v_\theta + \frac{t_E}{t_d}\frac{\partial \omega_z}{\partial r}, \tag{4.2}$$

where t_d is the diffusive time scale given by $t_d = (\sigma^2/\nu)^{1/2}$ (see Kloosterziel & van Heijst 1992). The last term simply represents horizontal diffusion due to viscosity. This equation is in non-dimensional form with the time scaled by the Ekman time scale t_E and not by t_a.

If the diffusive time scale is sufficiently long compared to the Ekman time scale, the diffusive term may be neglected, and the resulting equation,

$$\frac{\partial v_\theta}{\partial t} = -(1 + \omega_z/N)v_\theta, \tag{4.3}$$

represents the Ekman-layer effect. The first term on the right-hand side represents linear Ekman decay, familiar from quasi-geostrophic theory (cf. Pedlosky 1979). This term alone would only cause the profile to decay in amplitude everywhere at the same rate with no change in form. The nonlinear term, inversely proportional to N, is the correction for finite N introduced by Wedemeyer (1964). For anticyclones/cyclones, this term decreases/increases the decay rate. According to (4.3), the velocity profiles for anticyclones/cyclones evolve with the velocity maximum moving to a smaller/larger radius. The steepness of an anticyclone/cyclone will also decrease/increase. In fact, if we initialize equation (4.3) with a vorticity profile given by (2.1) the Ekman dynamics will cause the profile to evolve lower/higher gradients of vorticity in the anticyclonic/cyclonic case. Thus the effect of the nonlinear Ekman dynamics is to force anticyclones toward a more stable velocity profile and cyclones toward a more unstable profile.

Since the Wedemeyer theory is strictly valid only for axisymmetric flows at high $|N|$, we turned to our simulations at $|N| = 2$ to consider a detailed comparison. Comparing figures 12(*a*) and 12(*d*), we could see that in agreement with the Wedemeyer effect, the cyclone has decayed faster than the anticyclone. For a more detailed comparison with the theory, we took the v_θ field at the midpoint in the vertical direction (i.e. $z = \frac{1}{2}\pi$) and averaged in θ, thus producing a profile $\bar{v}_\theta(r)$ that we could compare to the results from (4.3). Quantitatively, the matches with theory were not very good. Qualitatively, the prediction about the direction of the shift of the velocity maximum holds up to about $t = 100 = 0.64t_E$. However, the prediction about the steepening of the velocity profile of the cyclonic vortex does not hold, since instead both cyclonic and anticyclonic profiles become more shallow.

On further investigation, we found a much better match between the theory and

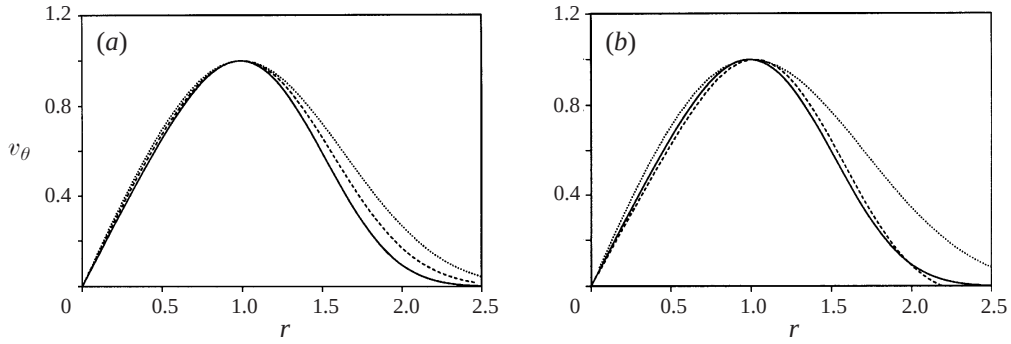

FIGURE 14. Velocity profiles $v_\theta(r)$. Each profile is normalized so that the maximum value is 1 and the position of the maximum is at $r = 1$. In each panel, the solid curve is the initial condition, while the dashed (dotted) curve is the profile at time $t = 100$ for the cases $N = +2$ ($N = -2$). Panel (a) shows the theoretical predictions and panel (b) gives the azimuthally averaged results from our simulations: (———, $t = 0$; – – – –, $t = 100$ for $N = 2$ ·····, $t = 100$ for $N = -2$)

experiment when we included the horizontal diffusion term in equation (4.2). The coefficient of the horizontal diffusion can be rewritten as

$$\frac{t_E}{t_d} = \frac{D}{\sigma}\frac{\sqrt{2}}{\left(Re|N|\right)^{1/2}}. \tag{4.4}$$

Thus for our case with $|N| = 2$ and $Re = 2500$, this ratio is $t_E/t_d \approx 0.063$, and this, it seems, is not small enough to neglect the explicit diffusive term in (4.2). In figure 13, we show the comparison between the theory with this diffusive term and the three-dimensional numerical simulations for $|N| = 2$ at times $t = 50, 100, 150$, and 200; that is for $t = 0.32t_E, 0.64t_E, 0.95t_E$, and $1.3t_E$. The correspondence is quite good for all times shown in the anticyclonic case, while for the cyclone, the comparison is good for the early and late times, with however some discrepancy for the intermediate times. Part of the discrepancy for the cyclonic case must be due to the early development of a tripolar anomaly which cannot be dealt with in the Wedemeyer theory.

The particularly pertinent prediction made by the Wedemeyer theory without the lateral diffusion that the cyclone profile will become steeper, may not hold if the diffusive term is important. To demonstrate this, we show in figure 14(a) the initial condition (the $\alpha = 3.5$ profile), and the $t = 100$ predictions for both cyclone and anticyclone. The curves are all normalized to have the same maximum value at the same radius to make them easier to compare. Under the action of both the nonlinear Ekman effect and the lateral diffusion, both cyclonic and anticyclonic profiles have become shallower. This is also seen in the data from the simulations shown in figure 14(b). This is in contrast to the results found in Kloosterziel & van Heijst (1992) where cyclonic vortices with an $\alpha = 2$ profile were found to steepen in the laboratory experiments. In that work, however, the ratio t_E/t_d was 4 to 5 times smaller than that used in the present study. In any case, we must conclude that an anticyclone with a stable profile (sufficiently small α) cannot be destabilized by the action of a nonlinear Ekman layer, and an initially unstable profile can be made stable by this effect. A cyclone can be destabilized by the Ekman-layer effect only if the lateral diffusion time scale is sufficiently longer than the Ekman time scale, otherwise lateral diffusion will dominate and make the cyclone more stable.

Under the conditions in our simulations, for $|N| = 2$, the cyclonic profile nearly retained its initial steepness while the anticyclone broadened considerably. This alone

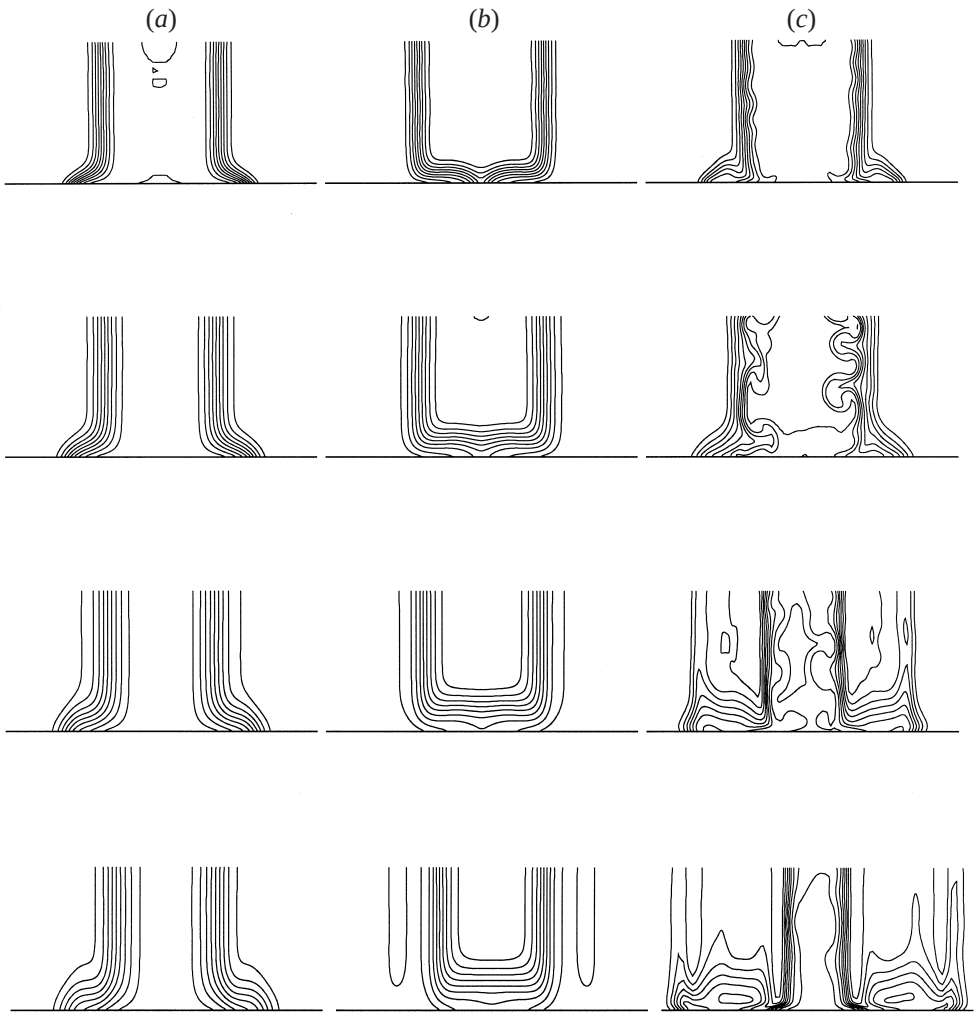

FIGURE 15. Iso-concentration contours of passive scalar in vertical sections passing through the point where ω_z takes its most negative value. (*a*) $N = -2$, (*b*) $N = +2$, (*c*) $N = -0.5$. From top to bottom $t = 50$, $t = 100$, $t = 150$, $t = 200$.

would suggest the possibility at $\alpha = 3.5$ for the cyclone to form an unstable tripole that breaks into dipoles, while it seemed in our example in figure 12(*d*) that the viscous decay was too rapid to allow the formation of an unstable tripole to proceed (the evolution was followed up to time $t = 250$). On the other hand, since the nonlinear Ekman effect causes the anticyclone to broaden, it is consistent to see the anticyclone transform into a stable tripole as in figure 12(*a*). For $\alpha = 3$ the anticyclonic broadening can be sufficient to stop the two-dimensional tripole formation with the structure remaining axially symmetric (as we saw in figure 10*c*), while the $\alpha = 3$ cyclone, maintaining its steepness, could become a tripole (as we saw in figure 11*b*).

The formation of the Ekman layer at the bottom of the vortex sets up a secondary circulation of flow which can be observed in the advection of a passive scalar. We have performed simulations with a passive scalar, with the ratio of kinematic viscosity to scalar diffusivity set at 1. In the laboratory experiments, the diffusivity of dyes typically used is three orders of magnitude smaller than the kinematic viscosity. Unfortunately

we cannot use such small diffusivity and still have the scalar field well resolved in our simulations. Even though our scalar field diffuses more rapidly than the dye in the tank, we believe we have been able to capture the important effects qualitatively. In figure 15, we show the evolution of a passive scalar field. The scalar was initially uniformly distributed within the core of the vortex, with a smooth transition to zero concentration in the negative-vorticity annulus, reaching zero about one third of the way between the points where the vorticity vanishes and where it is most negative. Comparing figures 15(*a*) ($N = -2$) and figure 15(*b*) ($N = +2$), it is evident that for the anticyclone/cyclone there is a radial outflow/inflow of fluid in the bottom boundary layer since the contour lines of the scalar, which are initially all vertical, bow out/in at the bottom of the anticyclone/cyclone. Note that in the cyclonic case, the resulting upward flux of passive scalar at the bottom continually raises the level of dye away from the bottom. This phenomenon is observed in the laboratory experiments when viewed from the side. Also, when viewed from above, it is possible to see that dye concentrated near the bottom of the tank will be drawn into a cyclone and not an anticyclone. A good illustration of this is given in Carnevale, Velasco Fuentes & Orlandi (1997*b*, figure 12). At the upper boundary we are imposing a free-slip condition on the flow and a non-diffusive condition (i.e. the normal derivative of scalar vanishes). In the laboratory experiments, however, there will also be a weak Ekman layer due to the water–air interface whose effect is not represented here. We are also neglecting the deformation of the free surface due to the presence of the vortex (cf. Maas 1993).

Figure 15(*c*) is shown as a representative case of the evolution of the scalar when there is centrifugal instability. Here in the scalar field at time $t = 100$ there is evidence of the overturning motion typical of this instability. By time $t = 150$ side cyclones have formed. It appears that passive scalar from the core anticyclone is being transferred through the bottom Ekman layer into the cyclones, which makes sense from the point of view of the simple linear Ekman-layer theory for the induced secondary circulation (i.e. axially downward in the anticyclone, radially out from the centre of the anticyclone in the Ekman layer, radially in toward the centres of the cyclones in the Ekman layer, and upward into the cyclone).

According to linear Ekman-layer theory (cf. Pedlosky 1979), the thickness δ_E of the layer should scale as

$$\delta_E = (\nu/|\Omega|)^{1/2}, \tag{4.5}$$

which can alternatively be written in terms the horizontal scale of the vortex as

$$\delta_E = \sigma \left(\frac{2}{|N|Re} \right)^{1/2}. \tag{4.6}$$

Thus for the case of $|N| = 2$, with $Re = 2500$, $\delta_E = \sigma/50$. We are able to resolve the Ekman layer in the simulations by using a variable mesh spacing with a relatively high density of grid points in the thin Ekman layer. In figure 16, we graph the radial velocity as a function of z at a radius of $r = 0.58$, which corresponds roughly to the position where v_r takes its maximum value (see figure 17) in the cases $N = \pm 2$ at time $t = 200$. As predicted by linear Ekman theory, the radial velocity in the Ekman layer is positive/negative for the anticyclone/cyclone. The radial velocity is maximum in magnitude near $z = \delta_E$ as given by equation (4.6). We have illustrated the grid mesh size by putting dots at the appropriate radii on the curve for the anticyclonic case. Including the boundary, there are 10 grid points from the wall to the point of maximum radial velocity, and another 18 in the region where the radial velocity

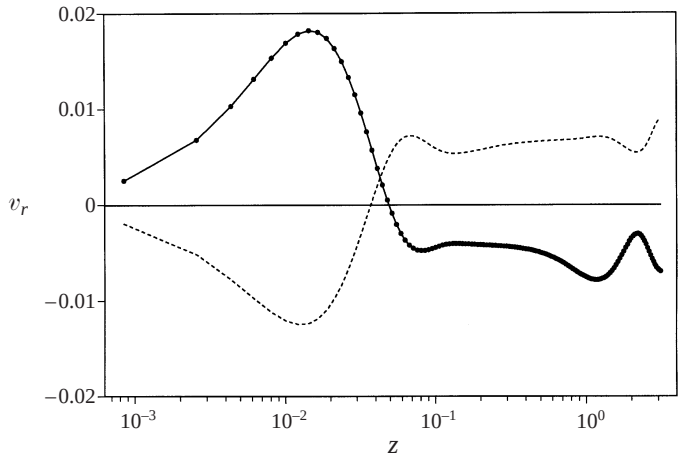

FIGURE 16. Radial velocity vertical profiles for ———, $N = -2$ and – – – –, $N = +2$. The profiles are logarithmic to emphasize the Ekman boundary layer region. The profiles are taken at $r = 0.58$, this position corresponding to the point of maximum of the radial velocity. On the solid lines the dots indicate the distribution of the computational grid points.

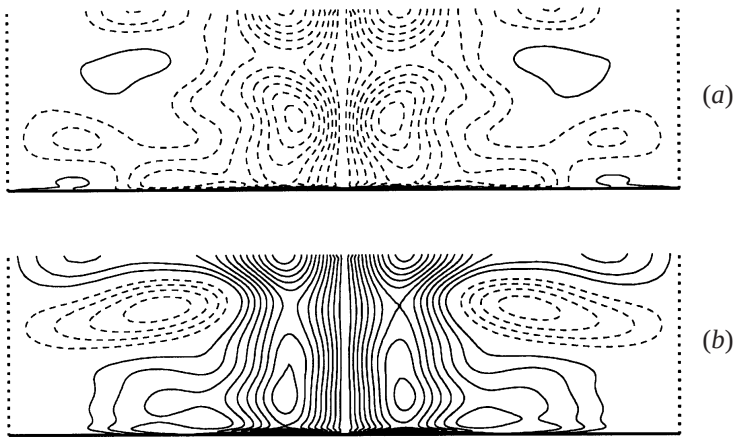

FIGURE 17. Contours of v_r at $t = 200$ in vertical sections that pass through the point where ω_z takes its most negative value; (*a*) $N = -2$, (*b*) $N = +2$ with $\Delta v_r = 0.001$,

decays to the interior value. The graphs give results that are qualitatively in accord with Ekman layer theory. Outside the Ekman layer, for the cyclone/anticyclone the radial velocity is weakly positive/negative, representing a slow outward/inward flow over most of the vortex column.

We also illustrate the radial velocity field over an entire vertical cross-sectional plane in figure 17 for the cases $N = \pm 2$. The orientation of the cross-section was chosen to pass through the position where $|\omega_r|$ achieves its maximum value. Note that on the scale of these plots the Ekman layer is so thin that it cannot be observed. The vertical velocity above the Ekman layer is small, with $|v_r|$ being at least an order of magnitude smaller than $|v_\theta|$ at the same position. Above the Ekman layer, the flow is outward/inward in the cyclone/anticyclone as predicted by linear Ekman theory.

In summary, we have examined in this section the effects of the Ekman boundary layer on the evolution of isolated vortices. Linear Ekman-layer theory alone is unable

to produce a quantitative match to the effect of the actual Ekman layer for the vortices unless N is very large. In the regime examined here, $|N| \leqslant 2$, the nonlinear Ekman effect introduced by Wedemeyer (1964) must be taken into account. This nonlinear effect causes cyclones to decay faster than anticyclones, as observed in our simulations. Also, in inviscid theory, the presence of this nonlinear effect means that as it evolves, the vorticity profile will become steeper/shallower for cyclones/anticyclones. Thus, the Wedemeyer effect cannot be responsible for triggering the barotropic instability in anticylones with initially stable profiles. In our simulations, we found a very poor quantitative match to the inviscid Wedemeyer theory predictions. The agreement was improved substantially by adding viscous effects to the theory. For the Reynolds number corresponding to our simulations, it turned out that both cyclones and anticyclones broaden in spite of the tendency of the inviscid Wedemeyer effect. Finally we showed evidence for the secondary flow induced by the Ekman layer, that is, in accord with linear Ekman layer theory, there is a flow toward (away from) the axis of the cyclone (anticyclone) in the Ekman layer. By mass conservation, this is accompanied by a corresponding outward (inward) radial flow from (toward) the axis of the cyclone (anticyclone) above the Ekman layer.

5. Discussion

In our investigation, we have tested several hypotheses based on laboratory observations concerning the differences between the evolution of cyclones and anticyclones in rotating flow. Here we review the relationship of our results to these hypotheses.

To begin with, it may be helpful to summarize briefly in table form the results of the two most important series of simulations that we presented above.

For the periodic boundary condition simulations with $\alpha = 3$ we have

N	
$-1, -0.75$	tripole formation not preceded by centrifugal instability
-0.66	weak centrifugal instability, tripole formation
-0.5	centrifugal instability, double-dipole instability
-0.33	centrifugal instability, transient quadrupole, double-dipole instability
$-0.1, 0$	centrifugal instability, turbulence
0.1	centrifugal instability, monopolar isolated vortex
0.175	weak centrifugal instability, tripole formation
$0.33, 0.5, 1$	no centrifugal instability, tripole formation

while for the simulations with a no-slip bottom boundary condition and $\alpha = 3.5$ we have

N	
$-2, -1$	tripole formation not preceded by centrifugal instability
-0.33	centrifugal instability, double-dipole instability
0.33	centrifugal instability, double-dipole instability
0.5	no centrifugal instability, unstable tripole formation
$1, 2$	no centrifugal instability, stable tripole formation

One of the main ideas that we tested was that centrifugal instability may be responsible for triggering the double-dipole or higher-order instabilities for anticyclonic vortices. Eliminating the Ekman layer effect from the problem (by using periodic boundary conditions), we were able to isolate the effect of the centrifugal

instability on the evolution of the vortices. We showed that beginning with a vorticity profile that is too 'shallow' ($\alpha = 3$) to result in the double-dipole centrifugal instability, the centrifugal instability produced 'rib' vortices that by vortex stretching enhanced the gradient of vertical vorticity, thus producing an azimuthal velocity profile that is sufficiently 'steep' to undergo double-dipole instability. The example that we gave in figure 7(*c*) even shows the formation of a transitory quadrupole state. We saw that this centrifugal instability was an effective means of producing the double-dipole instability only for a range of values of the rotation number more limited than the range of centrifugal instability. For more negative N, stable tripoles form. Note that stable tripoles were not observed to form from anticyclones in any of the laboratory experiments reported in the literature – a point to which we will return below. Another surprise was that the centrifugal instability in the cyclonic case with the same initial condition as in the anticyclonic case ($\alpha = 3$) did not produce the double-dipole instability. Instead, the centrifugal instability broadened the annulus of vorticity surrounding the core, thus resulting in a stable monopolar profile. The reason for this is not clear, especially when comparing two cases with very small $|N|$, as in figures 7(*a*) and 9(*a*). In the anticyclonic case, the rib vortices propagate deeply into the core, while in the cyclonic case they appear to be confined to the annulus (see figures 5*c* and 5*d*), even though the regions of instability are initially roughly the same (see figure 2).

Furthermore, by performing these periodic boundary condition simulations, we were able to refute a hypothesis concerning the relative amplitudes of vorticity in the tripole and double-dipole end states. The vortices start with a large difference in the magnitude of vorticity in the core of the vortex relative to the vorticity in the annulus. After tripole formation, this difference is preserved in that the magnitude of vorticity in the satellites is much lower than that in the core. For the double-dipole formation, however, the magnitude of the vorticity is comparable in all vortices. We have found that the centrifugal instability alone can produce this effect in the double-dipole instability. Thus it is not necessary to invoke the Ekman layer effect within the confining hollow cylinder in the laboratory experiments to explain this phenomenon (cf. Kloosterziel & van Heijst 1991).

In the simulations with Ekman damping, we were able to reproduce, at least qualitatively, all of the forms of instability observed in the experiments by choosing a sufficiently 'steep' initial profile $\alpha = 3.5$. Of particular interest is the formation of the unstable tripolar vortex from a cyclone (e.g. figure 12*c*). This can also be achieved for the periodic boundary condition case. It simply requires starting from a sufficiently steep profile. This is at odds with the suggestion given by van Heijst *et al.* (1991), that the formation of the unstable tripole was linked to the initial presence of a core vortex which itself was unstable. It seems more likely that in the case they reported the initial profile was steep and the effect of the satellites on the core then induced the observed unstable core structure, and not that the core was initially in itself unstable. At least we have shown that there is no need for a separate instability concerning the core to account for the result.

We have also addressed the question of the nonlinear Ekman layer effects related to the Wedemeyer (1964) equation by looking at two cases of relatively high rotation ($|N| = 2$). Since a nonlinear Ekman layer can make cyclonic vorticity profiles steeper, it was an attractive candidate for explaining why in the laboratory experiments it seems that cyclones always went unstable. However, the effect of horizontal diffusion of vorticity tends to broaden the vorticity profile and hence competes with the Ekman effect in this case. We showed that for reasonable values of the horizontal diffusion, the

combined effect of the Ekman layer and the horizontal diffusion simply maintained the steepness of the cyclonic profile. Thus to induce the tripole formation from a cyclone under these conditions requires having a sufficiently steep profile initially. To see the effect of the Ekman layer on steepening the vortex would require a much higher Reynolds number or much wider vortex than we have used (see (4.4)).

We found that the nonlinear Ekman effect according to the Wedemeyer (1964) equation makes the anticyclonic profiles shallower and hence more stable. Thus, as we showed in figure 9(*c*), it is possible to start with a barotropically unstable profile and have it stabilized by this effect, resulting in a monopolar final state. Also we note that we have observed the formation of a stable tripole from a barotropically unstable anticyclone. So, it seems that the Ekman layer effect cannot play a role in destabilizing anticyclones. Thus we are left to ask why were anticyclones always unstable in the laboratory experiments reported in the literature, and why their instabilities never produced a stable tripole. Our simulations would suggest two causes for this: either the initial profiles were too steep, or the centrifugal instability was too strong in the cases examined. Recently, the formation of a stable tripole from an anticyclone has been observed (Satijn & van Heijst, personal communication, 1998) lending support to this view. Our simulations did not address the formation of the initial condition in the laboratory, but this would be an interesting study in itself.

Our study was by necessity restricted in two regards that are undoubtedly of some importance in questions of vortex stability. One of these concerns the aspect ratio σ/D, which we have set at $1/\pi$. In the examples of centrifugal instability that we have analysed (e.g. those cases shown in figure 5), the vertical scale of the instability was somewhat smaller than σ. In those cases, D was probably sufficiently large to not have had a significant effect on the unfolding of the instability. However, one may expect that with D comparable to or smaller than σ the growth of the instability would be hampered. Thus a large aspect ratio may be stabilizing. The second effect that we did not deal with was that of free surface deformations. If one introduces gravity into the problem and allows the height of the upper surface to evolve, then cyclones and anticyclones will be affected differently. For example, the free surface will be depressed above cyclones and elevated above anticyclones. The degree to which free surface effects will be important can be measured by the Froude number, which for our basic vorticity profile we may define as $F = \omega_0\sigma/(gD)^{1/2}$. In the experiments described in Kloosterziel & van Heijst (1991, 1992), the Froude number so defined was small ($O(0.1)$), and we would suspect that the free surface effect played only a small role in the evolution. Maas (1993) shows that when F is not small, free surface effects will make the vorticity profile spread out which would suggest an improvement in stability, but all the implications of allowing the free surface to vary are not clear at this time. In any case, it does appear that the effects would be greater the larger the value of the aspect ratio.

Finally, we hope that the research reported here will stimulate additional laboratory studies, and we would encourage the use of three-dimensionalization visualization techniques which would be very useful in comparing with numerical simulations.

This research has been supported in part by Office of Naval Research grants N00014-96-1-0065 and N00014-97-1-0095 and National Science Foundation grant INT-9511552. We are grateful to Rudolf Kloosterziel for very helpful discussions and to Gert-Jan van Heijst for reading and commenting on an early version of the manuscript. Support from "Ministero dell 'Universita' e della Ricerca Scientifica" MURST MPI 60% grant and a CNR grant are also gratefully acknowledged.

REFERENCES

Cantwell, B. J. 1981 Organized motion in turbulent flow. *Ann. Rev. Fluid Mech.* **13**, 457–515.

Carnevale, G. F., Briscolini, M., Kloosterziel, R. C. & Vallis, G. K. 1997*a* Three-dimensionally perturbed vortex tubes in a rotating flow. *J. Fluid Mech.* **341**, 127–163.

Carnevale, G. F. & Kloosterziel, R. C. 1994 Emergence and evolution of triangular vortices. *J. Fluid Mech.* **259**, 305–331.

Carnevale, G. F. & Shepherd, T. G. 1990 On the interpretation of Andrew's theorem. *Geophys. Astrophys. Fluid Dyn.* **51**, 1–17.

Carnevale, G. F., Velasco Fuentes, O. U. & Orlandi, P. 1997*b* Inviscid dipole-vortex rebound from a wall or coast. *J. Fluid Mech.* **351**, 75–103.

Carton, X. J., Flierl, G. R. & Polvani, L. M. 1989 The generation of tripoles from unstable axisymmetric isolated vortex structures. *Europhys. Lett.* **9**, 339–344.

Carton, X. J. & Legras, B. 1994 The life-cycle of tripoles in two-dimensional incompressible flows. *J. Fluid Mech.* **267**, 53–82.

Carton, X. J. & McWilliams, J. C. 1989 Barotropic and baroclinic instabilities of axisymmetric vortices in a quasi-geostrophic model. In *Mesoscale/Synoptic Coherent Structures in Geophysical Turbulence* (ed. J. C. J. Nihoul & B. M. Jamart), pp. 225–244. Elsevier.

Drazin, P. G. & Reid, W. H. 1981 In *Hydrodynamic Stability*. Cambridge University Press.

Dritschel, D. G. 1988 Nonlinear stability bounds for inviscid, two-dimensional, parallel or circular flows with monotonic vorticity, and the analogous three-dimensional quasi-geostrophic flows. *J. Fluid Mech.* **191**, 575–581.

Flierl, G. R. 1988 On the instability of geostrophic vortices. *J. Fluid Mech.* **197**, 349–388.

Greenspan, H. P. 1980 *The Theory of Rotating Fluids*. Cambridge University Press.

Heijst, G. J. F. van & Kloosterziel, R. C. 1989 Tripolar vortices in a rotating fluid. *Nature* **338**, 569–571.

Heijst, G. J. F. van, Kloosterziel, R. C. & Williams, C. W. M. 1991 Laboratory experiments on the Tripolar vortex in a rotating fluid. *J. Fluid Mech.* **225**, 301–331.

Hua, B. L., Le Gentil, S. & Orlandi, P. 1997 First transitions in circular Couette flow with axial stratification. *Phys. Fluids* **9**, 365–375.

Kloosterziel, R. C. 1990 Barotropic vortices in a rotating fluid. PhD thesis, University of Utrecht.

Kloosterziel, R. C. & Carnevale, G. F. 1992 Formal stability of circular vorticese. *J. Fluid Mech.* **242**, 249–278.

Kloosterziel, R. C. & Heijst, G. J. F. van 1991 An experimental study of unstable barotropic vortices in a rotating fluid. *J. Fluid Mech.* **223**, 1–24.

Kloosterziel, R. C. & Heijst, G. J. F. van 1992 The evolution of stable barotropic vortices in a rotating free-surface fluid. *J. Fluid Mech.* **239**, 607–629.

Legras, B., Santangelo, P. & Benzi, R. 1988 High resolution numerical experiments for forced two-dimensional turbulence. *Europhys. Lett.* **5**, 37–42.

Libby, P. A. 1996 *Introduction to Turbulence*. Taylor & Francis, Washington, D.C.

Maas, L. R. M. 1993 Nonlinear and free-surface effects on the spin-down of barotropic vortices. *J. Fluid Mech.* **246**, 117–141.

Morel, Y. & Carton, X. 1994 Multipolar vortices in two-dimensional incompressible flow. *J. Fluid Mech.* **267**, 23–51.

Orlandi, P. & Fatica, M. 1997 Direct simulations of a turbulent pipe rotating along the axis. *J. Fluid Mech.* **343**, 43–72.

Orlandi, P. & Heijst, G. J. F. van 1992 Numerical simulation of tripolar vortices in 2D flow. *Fluid Dyn. Res.* **9**, 179–206.

Pedlosky, J. 1979 *Geophysical Fluid Dynamics*. Springer.

Smythe, W. D. & Peltier, W. R. 1994 Three-dimensional barotropic vortices on the f-plane. *J. Fluid Mech.* **265**, 25–64.

Verzicco, R. & Camussi, R. 1997 Transitional regimes of low-Prandtl thermal convection in a cylindrical cell. *Phys. Fluids* **9**, 1287–1295.

Verzicco, R., Lalli, F. & Campana, E. 1997 Dynamics of baroclinic vortices in a rotating, stratified fluid: a numerical study. *Phys. Fluids* **9**, 419–432.

Verzicco, R. & Orlandi P. 1996 A finite difference scheme for direct simulation in cylindrical coordinates. *J. Comput. Phys.* **123**, 402–414.

Wedemeyer, E. H. 1964 The unsteady flow within a spinning cylinder. *J. Fluid Mech.* **20**, 383–399.